

Peculiar velocity decomposition, redshift space distortion and velocity reconstruction in redshift surveys. II. Dark matter velocity statistics

Yi Zheng,¹ Pengjie Zhang,^{2,1,*} Yipeng Jing,² Weipeng Lin,¹ and Jun Pan³

¹*Key Laboratory for Research in Galaxies and Cosmology,*

Shanghai Astronomical Observatory, 80 Nandan Road, Shanghai, 200030, China

²*Center for Astronomy and Astrophysics, Department of Physics and Astronomy,*

Shanghai Jiao Tong University, 955 Jianchuan road, Shanghai, 200240

³*National Astronomical Observatories, Chinese Academy of Sciences,*

20A Datun Road, Chaoyang District, Beijing 100012, P. R. China

Massive spectroscopic redshift surveys open a promising window to accurately measure peculiar velocity at cosmological distances through redshift space distortion (RSD). In Paper I [1] of this series of work, we proposed decomposing peculiar velocity into three eigenmodes (\mathbf{v}_δ , \mathbf{v}_S and \mathbf{v}_B) in order to facilitate the RSD modeling and peculiar velocity reconstruction. In the current paper we measure the dark matter RSD-related statistics of the velocity eigenmodes through a set of N-body simulations. These statistics include the velocity power spectra, correlation functions, one-point probability distribution functions, cumulants, and the damping functions describing the Finger of God effect. We have carried out a number of tests to quantify possible numerical artifacts in these measurements and have confirmed that these numerical artifacts are under control. Our major findings are as follows: (1) The power spectrum measurement shows that these velocity components have distinctly different spatial distribution and redshift evolution, consistent with predictions in Paper I. In particular, we measure the window function $\tilde{W}(k, z)$. \tilde{W} describes the impact of nonlinear evolution on the \mathbf{v}_δ -density relation. We confirm that the approximation $\tilde{W} = 1$ can induce a significant systematic error of $O(10\%)$ in RSD cosmology. We demonstrate that \tilde{W} can be accurately described by a simple fitting formula with one or two free parameters. (2) The correlation function measurement shows that the correlation length is $O(100)$, $O(10)$, and $O(1)$ Mpc for \mathbf{v}_δ , \mathbf{v}_S , and \mathbf{v}_B respectively. These correlation lengths determine where we can treat the velocity fields as spatially uncorrelated. Hence, they are important properties in RSD modeling. (3) The velocity probability distribution functions and cumulants quantify non-Gaussianities of the velocity fields. We confirm speculation in Paper I that \mathbf{v}_δ is largely Gaussian, but with non-negligible non-Gaussianity. We confirm that \mathbf{v}_B is significantly non-Gaussian. We also measure the damping functions. Despite the observed non-Gaussianities, the damping functions and hence the Finger of God effect are all well approximated as Gaussian ones at scales of interest.

PACS numbers: 98.80.-k; 98.80.Es; 98.80.Bp; 95.36.+x

I. INTRODUCTION

Redshift space distortion (RSD) is emerging as a powerful probe of dark energy and gravity at cosmological scales [2–35]. However, RSD modeling is highly complicated (e.g., [36–41] and references therein), due to entangled nonlinearities in the velocity and density fields and in the real space-redshift space mapping.

RSD is induced by peculiar motion. Naturally the first step to understand RSD is to understand the peculiar velocity \mathbf{v} . It turns out that different components of \mathbf{v} affect RSD in different ways. Motivated by it, we proposed a unique decomposition of \mathbf{v} into three eigenmodes (Paper I, [1]). The three components are not only uniquely defined mathematically, but also have unique physical meanings and have different impacts on RSD. We find that this decomposition indeed facilitates the RSD modeling. It helps us in arriving at a new RSD formula. It also helps us in proposing new approaches to reconstruct

three-dimensional peculiar velocity at cosmological distances through spectroscopic redshift surveys.

Paper I outlined the basic methodology, but left most quantitative analysis for future studies. The present paper (Paper II) is the second paper of the series, focusing on the RSD-related dark matter velocity statistics. Future works will extend to the halo velocity statistics and eventually to the galaxy velocity statistics. We will evaluate the accuracy of the proposed RSD formula for dark matter and galaxies. We will also investigate the proposed velocity reconstruction techniques.

This paper is organized as follows. §II briefly describes the three velocity components. §III describes the simulations and the velocity assignment method used for the analysis. Numerical artifacts are quantified through several tests detailed in the Appendix and are proven to be under control. §IV shows the results of relevant velocity statistics. We summarize and discuss in §V.

*Email me at: zhangpj@sytu.edu.cn

II. THEORY BASICS

Paper I proposed decomposing the velocity \mathbf{v} into three eigenmodes (\mathbf{v}_δ , \mathbf{v}_S , and \mathbf{v}_B). This decomposition allows us to conveniently derive the leading-order RSD corrections in the redshift space power spectrum. For the dark matter redshift space power spectrum,

$$P_{\delta\delta}^s(k, u) \simeq \left(P_{\delta\delta}(k) \left(1 + f\tilde{W}(k)u^2 \right)^2 \right. \\ \left. + u^4 P_{\theta_S\theta_S}(k) + C_G(k, u) + C_{NG,3}(k, u) \right) \\ \times D^{\text{FOG}}(ku). \quad (1)$$

Here, $u \equiv k_z/k$. The FOG effect is described by the damping function

$$D^{\text{FOG}}(ku) = D_\delta^{\text{FOG}}(ku) D_S^{\text{FOG}}(ku) D_B^{\text{FOG}}(ku). \quad (2)$$

We predict in paper I that \mathbf{v}_B only contributes to the Finger of God (FOG) effect through D_B^{FOG} . \mathbf{v}_S causes both an enhancement ($P_{\theta_S\theta_S}$) and a damping (D_S^{FOG}). All other terms in Eq. (1) are contributed by \mathbf{v}_δ . For more details, refer to Paper I. Here we just summarize the basic results of the three velocity components, with terms in Eq. (1) explained.

\mathbf{v}_δ is irrotational ($\nabla \times \mathbf{v}_\delta = 0$) and is completely correlated with the underlying density field δ . The relation in Fourier space is

$$\theta_\delta(\mathbf{k}) = \delta(\mathbf{k})W(\mathbf{k}), \quad (3) \\ W(\mathbf{k}) = W(k) = \frac{P_{\delta\theta}(k)}{P_{\delta\delta}(k)}.$$

Here, $\theta_\delta \equiv -\nabla \cdot \mathbf{v}_\delta/H$ and $\theta \equiv -\nabla \cdot \mathbf{v}/H$. P_{AB} is the power spectrum between the field A and the field B , defined as $\langle A(\mathbf{k})B(\mathbf{k}') \rangle \equiv (2\pi)^3 \delta_{3D}(\mathbf{k} + \mathbf{k}') P_{AB}(\mathbf{k})$. We often use the notation $\Delta_{AB}^2 \equiv k^3 P_{AB}/(2\pi^2)$, which enters into the ensemble average $\langle A(\mathbf{x})B(\mathbf{x}) \rangle = \int \Delta_{AB}^2(k) dk/k$. If A and B are vector fields, $\langle AB \rangle \rightarrow \langle \mathbf{A} \cdot \mathbf{B} \rangle$.

In the limit $k \rightarrow 0$, $W \rightarrow f \equiv d \ln D / d \ln a$ for the matter field [64]. Here, D is the linear density growth factor. Clearly \mathbf{v}_δ contains most information of RSD cosmology. Nonlinear evolution causes W at small scales to deviate from the linear theory prediction. Such deviation is described by the dimensionless

$$\tilde{W}(k) \equiv \frac{W(k)}{f(k)}. \quad (4)$$

This definition is slightly different from that in Paper I. But for Λ CDM, in which f is scale independent, the two definitions are identical. But in modified gravity models or in models with dark energy fluctuations, f is scale dependent. \tilde{W} defined in this way, hence, isolates the impact of nonlinear evolution from the scale dependence in linear evolution. We expect $\tilde{W} \leq 1$ in general, even for modified gravity models and models with dark energy fluctuations.

We find that \tilde{W} can deviate from unity by $\sim 1-10\%$ at $k = 0.1h/\text{Mpc}$. It modifies the Kaiser formula (for dark matter RSD) from $P_{\delta\delta}(1 + fu^2)^2$ to $P_{\delta\delta}(1 + f\tilde{W}u^2)^2$. So if the \tilde{W} is not taken into account, f can be biased low by $\sim 10\%$, as predicted by perturbation theory. A systematic error of such amplitude is severe for stage IV dark energy surveys like BigBOSS/MS-DESI [42], CHIME [43], Euclid [44] and SKA [45]. In the present paper we will quantify \tilde{W} more robustly, through N-body simulations.

\mathbf{v}_δ causes both large-scale enhancement and small-scale damping in the redshift space clustering. Besides the \tilde{W} correction, nonlinearities in \mathbf{v}_δ induce complicated high order corrections (C_G and C_{NG}) to the Kaiser effect in RSD modeling (Paper I). These high-order corrections involve both the velocity and density fields, so quantifying them is beyond the scope of this paper and will be left for future investigation through N-body simulations. In principle, nonlinearities in \mathbf{v}_δ also complicate the FOG effect.

\mathbf{v}_S is also irrotational ($\nabla \times \mathbf{v}_S = 0$). But to the opposite of \mathbf{v}_δ , it is uncorrelated with the underlying density field ($\langle \theta_S(\mathbf{x})\delta(\mathbf{x} + \mathbf{r}) \rangle = 0$). This velocity component arises from nonlinear evolution. It is the cause of density-velocity stochasticity,

$$r_{\delta\theta}(k) \equiv \frac{P_{\delta\theta}(k)}{\sqrt{P_{\delta\delta}(k)P_{\theta\theta}(k)}} = \frac{1}{\sqrt{1 + \eta(k)}}, \quad (5) \\ \eta(k) \equiv \frac{P_{\theta_S\theta_S}(k)}{P_{\theta_S\theta_S}(k)}.$$

\mathbf{v}_S causes both large-scale enhancement and small-scale damping in the redshift space clustering. But notice that the leading-order large-scale enhancement has a u^4 angular dependence [Eq. (1)]. It hence differs significantly from the Kaiser effect.

\mathbf{v}_B is the curl (rotational) component, satisfying $\nabla \cdot \mathbf{v}_B = 0$. \mathbf{v}_B grows only after orbit crossing occurs. We expect its power to concentrate at small scales. We also expect that, to a good approximation, it only damps the redshift space clustering and only induces the FOG effect.

The present paper aims to quantify the RSD-related statistics of the three velocity components, through simulations. These statistics include

- the power spectra $\Delta_{v_\alpha v_\alpha}^2 \equiv P_{v_\alpha v_\alpha} k^3 / (2\pi^2)$,
- $\tilde{W}(k, z)$ and in particular the $\tilde{W}(k, z)$ - $\Delta_{\delta\delta}^2(k, z)$ relation,
- the correlation functions $\psi_{\perp, v_\alpha v_\alpha}(r, z)$ and $\psi_{\parallel, v_\alpha v_\alpha}(r, z)$,
- $P(v_{z,\alpha})$, the probability distribution functions (PDFs) of \mathbf{v}_α along the z axis, and their derived properties such as cumulants and the FOG function D_α^{FOG} .

Here, the subscript $\alpha = \delta, S, B$ denotes the three velocity components.

III. N-BODY SIMULATION AND VELOCITY ASSIGNMENT METHOD

Given the involved nonlinearities, N-body simulations are needed to robustly quantify the above velocity statistics. Furthermore, comprehensive tests must be designed and performed to robustly quantify numerical artifacts associated with simulations themselves and numerical artifacts associated with the velocity assignment method.

A. N-body simulations

From the structure formation theory, we expect that \mathbf{v}_δ dominates at linear/large scales while \mathbf{v}_S and \mathbf{v}_B become important at sufficiently nonlinear/small scales. Given the computation limitation, it would be difficult for a single simulation to robustly evaluate all three components. A natural remedy is to combine large box simulations with small box simulations. Large box simulations help us better understanding the velocity field at large scales, in particular \mathbf{v}_δ . Small box simulations have high mass and force resolution, so they can probe \mathbf{v}_S and \mathbf{v}_B more robustly. Combining these results, we can then circumvent the computation limitation and accurately study the statistical properties of the three velocity components.

For this reason, we combine three high-resolution (particle number $N_P = 1024^3$) dark matter simulations with box size $L_{\text{box}}/h^{-1}\text{Mpc} = 1200, 300, \text{ and } 100$. For brevity, we will refer to them as J1200, J300, and G100, respectively. The simulations utilize standard ΛCDM cosmology with flat space and Gaussian initial conditions. Simulation specifications are listed in Table I. The adopted cosmological parameters are identical, expect a slight difference in the baryon density Ω_b . For the purpose of our work, we can safely neglect this difference. J1200 and J300 are run with a particle-particle-particle-mesh (P³M) code (see [46] for details). G100 is run with Gadget2 [47, 48]. For J1200 and G100, we analyze four redshift snapshots, respectively, which are $z = 0, 0.501, 1.074, 1.878$, of J1200 and $z = 0, 0.526, 1.024, 1.947$, of G100. Some output redshifts of J1200 differ from corresponding ones of G100 by $\Delta z/(1+z) \lesssim 3\%$. The linear velocity growth rate is fHD , where $f \equiv d \ln D / d \ln a$ and D is the linear den-

Name	$L_{\text{box}}/h^{-1}\text{Mpc}$	N_P	$m_P/h^{-1}M_\odot$	Ω_b
J1200	1200	1024^3	1.2×10^{11}	0.045
J300	300	1024^3	1.9×10^9	0.045
G100	100	1024^3	6.7×10^7	0.044

TABLE I: Specifications of the three simulations. Except for the slightly different Ω_b , all three have $\Omega_m = 0.268$, $\Omega_\Lambda = 0.732$, $\sigma_8 = 0.85$, $n_s = 1$, and $h = 0.71$. The slight difference in Ω_b is negligible for the velocity statistics presented in this paper. N_P is the total particle number and m_P is the mass of each simulation particle.

sity growth factor. So these differences in z result in $\sim \frac{1}{2}\Delta z/(1+z) \lesssim 1.5\%$ [65] in velocity. The major purpose of this paper is to identify the three velocity components and their basic statistics. For this purpose we can safely neglect these redshift differences in the current paper. For brevity we refer to the four snapshots as $z = 0.0, 0.5, 1.0, 2.0$ hereafter. Nevertheless, eventually we need to analyze simulations at identical redshifts. We also need to run many realizations to robustly quantify the velocity statistics. For J300, we only analyze its $z = 0$ snapshot since it is mainly used to test our velocity assignment method in the Appendix (Fig. 12).

B. The velocity assignment method

It is tricky to properly estimate the volume-weighted velocity field from velocities of inhomogeneously distributed dark matter particles or galaxies (e.g. [49] and references therein). In N-body simulations, we only have limited simulation particles and only have the velocity information at positions of these particles. However, the velocity where there is no particle is not necessarily small/negligible. In contrast, since the velocity is determined by the large-scale matter distribution, velocity in low-density regions/voids can be large and in general non-negligible. This sampling bias is difficult to correct from first principles, especially due to the awkward situation that the velocity and density fields are neither completely correlated nor completely uncorrelated.

We take a simple procedure to estimate the volume weighted velocity field in simulations. For a given grid point, we assign the velocity of its nearest dark matter particle/halo/galaxy to it. We call this method the nearest-particle (NP) method. The probability P for a particle's velocity to be assigned to a grid is inversely proportional to its ambient particle number density n_P , $P \propto 1/n_P \propto V$, where V denotes the volume it occupies. So the NP velocity assignment method indeed constructs a volume-weighted velocity field [66].

We emphasize that this velocity assignment method is different to the widely used nearest-grid-point (NGP) method in constructing the density field. For NGP, each particle looks for its nearest grid point and assigns itself to this grid point. All particles are used in the assignment. But for NP, each grid point looks for its nearest particle and is assigned with the particle velocity. In dense regions, only a fraction of particles are used in the assignment. In underdense regions, some particles are used repeatedly and their velocities are assigned to more than one grid point. In this sense, it does not use all information of particles. A simple remedy is to shift the grids so another set of particles is used for the velocity assignment.

We also emphasize the difference between the NP method and the Voronoi tessellation (VT) method [49]. The first step of the VT method is to fill the space with polyhedral cells. Each polyhedron contains only one par-

ticle, and it covers all space points who consider this particle to be their nearest particle. The velocity within this polyhedron is assigned to be the velocity of that particle. The next step is to smooth the velocity field over a given window function to obtain the velocities on regular grids. We realize that the NP method is essentially the first step of the VT method. However, unlike the VT method, the NP method does not apply a smoothing. This is to avoid artificial suppression of small-scale random motions, which are *real signals* of significant impact on the FOG effect. This artificial suppression of small scale velocity components also exists in the widely adopted Delaunay tessellation (DT) method [49–51]. This is the major reason that we do not adopt this method [67].

The NP method is straightforward to implement. Furthermore, it is robust in a number of aspects, despite its simplicity: (1) In high-density regions, NP does not cause underestimation in the (one-dimensional) velocity dispersion $\sigma_v \equiv \sqrt{\langle v^2 \rangle}$, since it does not average over particle velocities. This is important for RSD study, otherwise, underestimation of σ_v will cause underestimation of FOG. (2) It robustly measures \mathbf{v}_δ , which is of the most importance for RSD cosmology. For the NP velocity assignment, high-density regions are no problem because there are always particles within a grid size. In underdense regions, the typical distance from a given grid point to its nearest particle is $(1+\delta)^{-1/3} L_{\text{Box}}/N_P^{1/3}$, which can be large. But in such regions \mathbf{v}_δ does not vary strongly, since its typical length L of variation is roughly given by $|v/L| = |\delta WH|$ [Eq. (3)]. The requirement to robustly sample \mathbf{v}_δ is then

$$\begin{aligned} \frac{L_{\text{Box}}}{N_P^{1/3}} &< \left| \frac{v}{HW} \frac{(1+\delta)^{1/3}}{\delta} \right| \\ &= 3\text{Mpc}/h \frac{|v|}{300\text{km}/s} \frac{1}{f} \frac{1}{\bar{W}} \frac{H_0}{H} \left| \frac{(1+\delta)^{1/3}}{\delta} \right|. \end{aligned} \quad (6)$$

This condition is not difficult to satisfy for typical simulation specifications today. For example, for our J1200 simulation, $L_{\text{Box}}/N_P^{1/3} = 1.2 \text{ Mpc}/h$ and the above condition is usually satisfied. Notice that $\tilde{W} \leq 1$ and $f \leq 1$ ($f \simeq 0.5$ at $z = 0$). An exception is the very underdense regions with $\delta \lesssim -0.99$. In these regions, our simulation undersamples the \mathbf{v}_δ field. But these regions are very rare and we do not expect this undersampling to be severe for statistically evaluating the \mathbf{v}_δ field. (3) The NP method does not use the velocity information of all particles. Nevertheless, the information encoded in unused particles can be captured by shifting the grids and resampling the velocity field, when necessary.

C. The velocity decomposition method

After sampling the velocity field \mathbf{v} on regular grids by the NP method, we proceed to decompose \mathbf{v} into the three eigenmodes. The velocity decomposition is conve-

niently operated in Fourier space. First we make the E/B decomposition,

$$\begin{aligned} \mathbf{v}_E(\mathbf{k}) &= \frac{(\mathbf{k} \cdot \mathbf{v}(\mathbf{k}))}{k^2} \mathbf{k}, \\ \mathbf{v}_B(\mathbf{k}) &= \mathbf{v}(\mathbf{k}) - \mathbf{v}_E(\mathbf{k}). \end{aligned} \quad (7)$$

Then we decompose \mathbf{v}_E into \mathbf{v}_δ and \mathbf{v}_S [Eq. (3)] [68],

$$\begin{aligned} \mathbf{v}_\delta(\mathbf{k}) &= -i \frac{H(z)\delta(\mathbf{k})W(k)}{k^2} \mathbf{k}, \\ \mathbf{v}_S(\mathbf{k}) &= \mathbf{v}_E(\mathbf{k}) - \mathbf{v}_\delta(\mathbf{k}). \end{aligned} \quad (8)$$

Here $H(z)$ is the Hubble parameter at redshift z , and the window function W is calculated in advance by $W = P_{\delta\theta}/P_{\delta\delta}$. The density field δ is sampled by the NGP method on the same regular grids as the velocity field. When calculating $P_{\delta\delta}$, we do not correct the shot noise term since it is negligible for our high particle number density simulation. Also we do not correct other numerical artifacts like smoothing and alias effects, which are subdominant to systematic errors induced by the velocity assignment method. Hence, numerical artifacts quantified by our designed tests (Appendix A) receive minor contribution from those in the density field.

D. Testing the NP method

In Appendix A we design and carry out several tests to verify the robustness of the NP method for our study.

First we compare the power spectra of the three velocity components between different box sizes, grid numbers, and particle numbers. Discrepancies there diagnose sampling bias. In particular, the NP method becomes exact in the limit $N_P/L_{\text{box}}^3 \rightarrow \infty$. By constructing the velocity field using a fraction of particles and observing its dependence on the particle numbers, we can evaluate its accuracy. If the results converge, we then have confidence of vanishing sampling bias. Detailed comparison is given in Appendix A.

In brief, we find that NP method can construct \mathbf{v}_δ and \mathbf{v}_S fields quite reliably. However, for large box simulations (e.g. J1200), the \mathbf{v}_B amplitude is significantly overestimated at all scales due to a shot-noise-like alias effect induced by sparse sampling [51]. However, tests on small box simulation G100 show reasonable convergence of \mathbf{v}_B . So the G100 simulation provides reasonably accurate measure of \mathbf{v}_B . Hence, in combination of J1200 and G100, we have reliable measures of all three velocity components.

We also test the NP method against the fiducial velocity field of known statistics as input (§A2). This test is particularly good at highlighting leakage between the three velocity components. We do find such leakages. We quantify their amplitudes as a function of scales and identify regions where these leakages are under control.

These tests show that, combining J1200 and G100, we can control numerical artifacts and reliably measure all

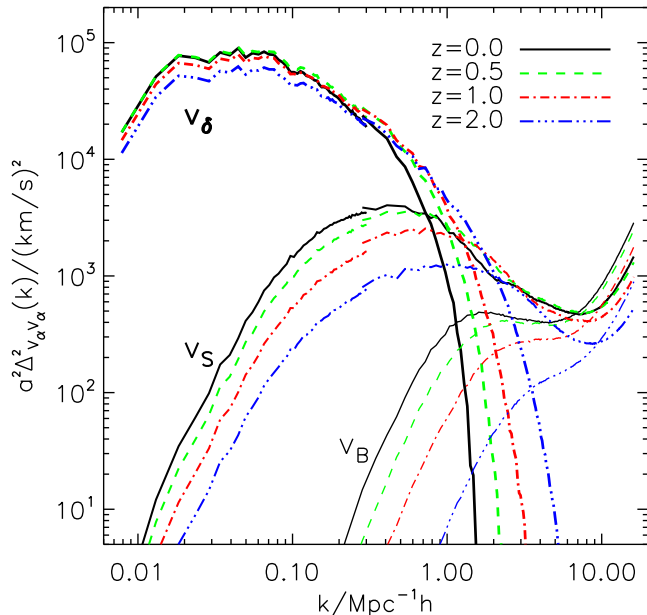


FIG. 1: The proper velocity power spectrum $a^2 \Delta^2_{v_\alpha v_\alpha}(k, z)$ ($\alpha = \delta, S, B$) at $z = 0, 0.5, 1.0, 2.0$. As a note, all symbols of \mathbf{v} in Paper I and this paper refer to the *comoving* peculiar velocity. But in order to better show the redshift evolution, we plot the physical velocity power spectra $a^2 \Delta^2_{v_\alpha v_\alpha}$ instead. The thick, intermediate thick, and thin lines represent $a^2 \Delta^2_{v_\delta v_\delta}(k, z)$, $a^2 \Delta^2_{v_S v_S}(k, z)$, and $a^2 \Delta^2_{v_B v_B}(k, z)$, respectively. We combine the J1200 simulation and the G100 simulation to reduce numerical artifacts. $a^2 \Delta^2_{v_\delta v_\delta}$ and $a^2 \Delta^2_{v_S v_S}$ at $k < 0.3h/\text{Mpc}$ are from J1200, while those of $k > 0.3h/\text{Mpc}$ are from G100. $a^2 \Delta^2_{v_B v_B}$ is from G100. As shown in this figure, $a^2 \Delta^2_{v_\delta v_\delta}$ at $z = 0$ and $z = 0.5$ overlap largely. This is because $a\mathbf{v}_\delta$ ceases to grow after $z \simeq 0.2$ as the cosmological constant slows down the structure growth. Unless otherwise specified, the measurement is done on $N_{\text{grid}} = 512^3$ grid.

three velocity components. Even better, the impacts of these numerical artifacts on RSD cosmology are further reduced for a number of reasons. First, the majority of cosmological information resides in relatively large scales and especially in \mathbf{v}_δ . This component is accurately measured. Second, although accurate measurement of \mathbf{v}_B is more challenging, its impact on RSD is fully captured by its velocity dispersion σ_{v_B} (Sec. IV), which can be treated as a free parameter to be fitted against data. Even simpler, Sec. IV will show that setting $\sigma_{v_B} = 0$ is already sufficiently accurate for RSD modeling.

IV. STATISTICS OF $\mathbf{v}_{\delta, S, B}$

Understanding the statistical properties of the three velocity components facilitates the RSD modeling and velocity reconstruction (Paper I). For this purpose, we measure the one-point and two-point velocity statistics from

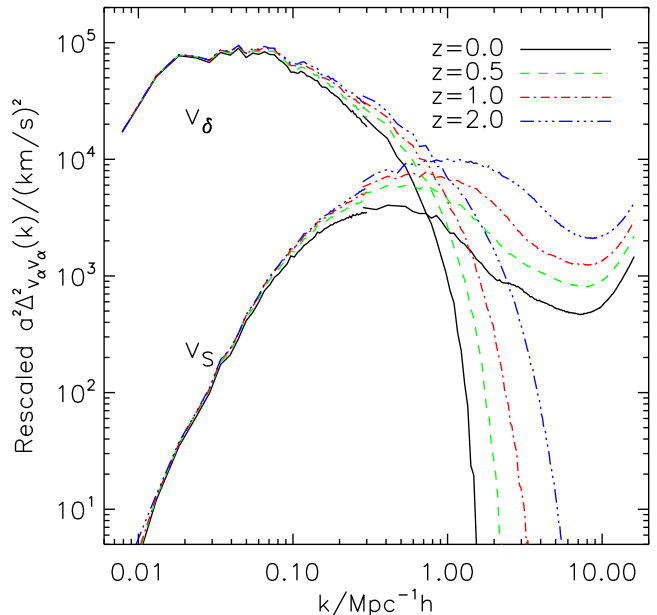


FIG. 2: Rescaled $a^2 \Delta^2_{v_\delta, S, v_\delta, S}$ to demonstrate their redshift evolution. (1) $\Delta^2_{v_\delta v_\delta}(z)$ is rescaled by the linear velocity growth factor $D_{v_\delta}^2(z=0)/D_{v_\delta}^2(z)$ [Eq. (9)]. Nonlinear evolution is visible at $k \gtrsim 0.03h/\text{Mpc}$ and becomes non-negligible at $k \gtrsim 0.1h/\text{Mpc}$. (2) $\Delta^2_{v_S v_S}(z)$ is rescaled by the third-order perturbation prediction $(D^2 fH)^2(z=0)/(D^2 fH)^2(z)$ [Eq. (11)].

simulations. (1) The velocity power spectra $\Delta^2_{v_\alpha v_\alpha}(k, z)$ ($\alpha = \delta, S, B$) go directly into the redshift space matter power spectrum. They also quantify the scale dependence and redshift evolution of these velocity components. They are useful to understand the physical origins of these velocity components. The window function W is a derived quantity of these power spectra. (2) Velocity correlation functions $\psi_{\parallel, v_\alpha v_\alpha}$ and $\psi_{\perp, v_\alpha v_\alpha}$ ($\alpha = \delta, S, B$) quantify the velocity correlation length, L_α . These correlation lengths are crucial in judging at which separation we can treat the velocities at two positions as independent. Basically, if the scale of interest $k \ll 2\pi/L_\alpha$, we can safely ignore the intrinsic clustering of the \mathbf{v}_α field. In this limit, we can treat \mathbf{v}_α as a random field in RSD modeling, whose impact is fully captured by a damping function D_α^{FOG} . Otherwise, we have to take their intrinsic clustering into account, which contributes extra power to the redshift space clustering. (3) Finally, we will quantify the non-Gaussianities of the velocity fields, through the one-point PDF and the reduced cumulants K_j . These non-Gaussianity measures are highly relevant for modeling D_α^{FOG} , which describes the FOG effect.

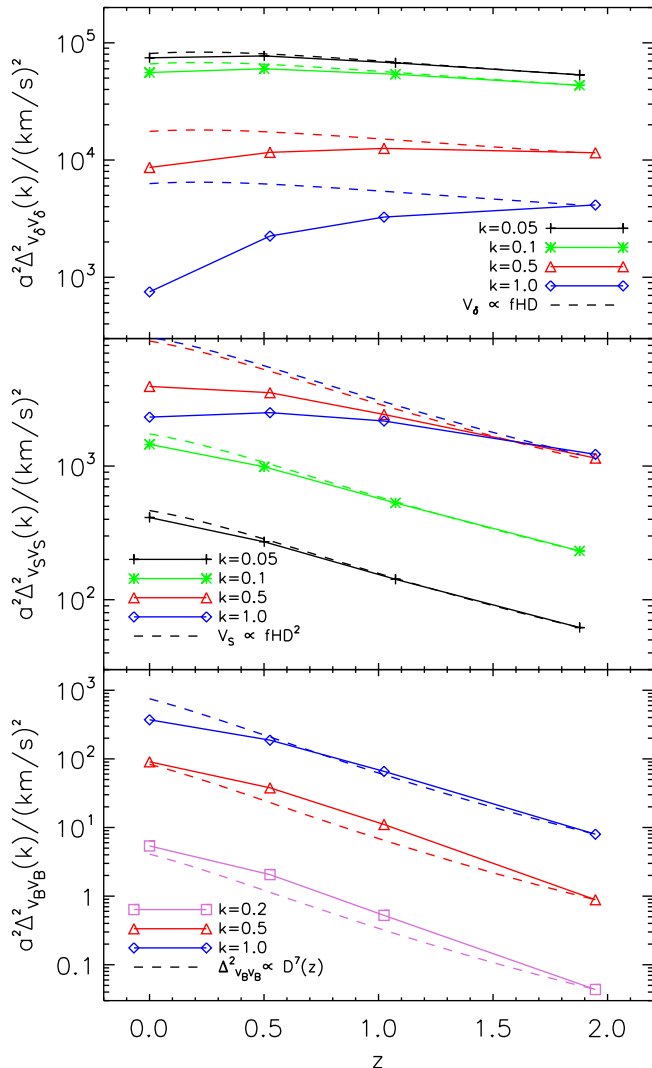


FIG. 3: Redshift evolution in $\Delta_{v_\alpha v_\alpha}^2$ ($\alpha = \delta, S, B$). Dashed lines correspond to predictions of the linear perturbation theory ($\mathbf{v}_\delta \propto fHD$), third-order perturbation theory ($\mathbf{v}_S \propto fHD^2$), and the finding by [51] on \mathbf{v}_B ($\Delta_{v_B v_B}^2 \propto D^7$).

A. The velocity power spectrum

The velocity power spectra at $z = 0.0, 0.5, 1.0, 2.0$ are shown in Fig. 1. These results confirm our speculation in Paper I, based upon the structure formation theory. It shows that \mathbf{v}_δ is the dominant component at linear and mildly nonlinear scales. Perturbation theory predicts that it evolves linearly at sufficiently large scales, with the linear velocity growth factor

$$D_{v_\delta}(z) = f(z)H(z)D(z). \quad (9)$$

Figures. 2 and 3 verify this linear evolution at $k < 0.1h/\text{Mpc}$. However, linear perturbation theory quickly loses its predicting power at $k > 0.1h/\text{Mpc}$. Even at $k = 0.1h/\text{Mpc}$, impact of nonlinear evolution is visible.

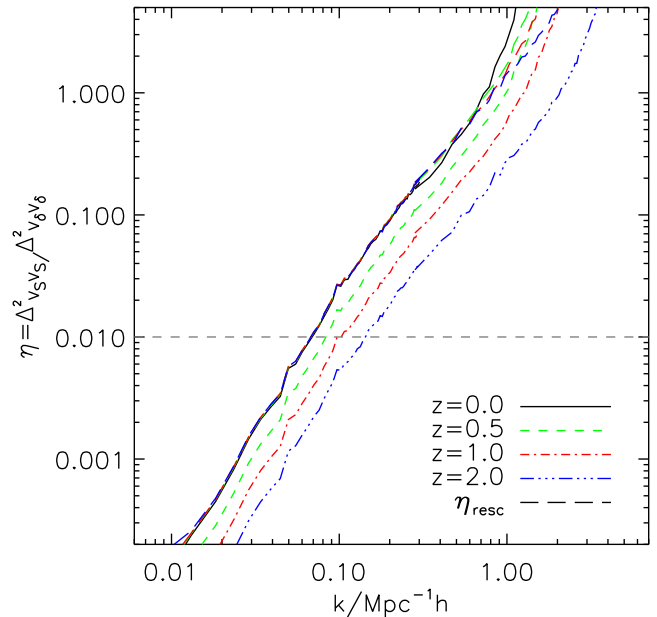


FIG. 4: $\eta \equiv P_{v_S v_S} / P_{v_\delta v_\delta}$ is shown at $z = 0, 0.5, 1.0, 2.0$. η quantifies the velocity-density stochasticity ($r_{\delta\theta} = 1/\sqrt{1+\eta}$). It also shows the relative importance of \mathbf{v}_S with respect to \mathbf{v}_δ . Future surveys require 1% accuracy in RSD modeling and hence require the inclusion of \mathbf{v}_S at $k \gtrsim 0.1h/\text{Mpc}$. To compare with the perturbation theory prediction ($\eta \propto D^2$), we plot $\eta_{resc} = \eta(z) \times D^2(z=0)/D^2(z)$ (long dashed lines). The prediction works well such that the rescaled lines largely overlap with each. We find that, to a good approximation, $\eta(k, z) \propto D^2(z)k^{n_\eta}$, with $n_\eta \simeq 2.2$ at $k \lesssim 0.7h/\text{Mpc}$.

Nonlinear evolution in the velocity and density fields drive $\tilde{W} \equiv W/f$ to decrease from unity. \tilde{W} is one of the most important properties to describe the velocity field, to model RSD, and to reconstruct velocity in spectroscopic surveys. Hence we devote the whole Sec. IV B to discuss it.

Nonlinear evolution also induces stochasticity in the velocity-density relation and causes the emergence of \mathbf{v}_S (Fig. 1). It eventually dominates over \mathbf{v}_δ at $k = 1h/\text{Mpc}$ and $z = 0$. To better show its impact, Fig. 4 plots the ratio $\eta \equiv P_{v_S v_S} / P_{v_\delta v_\delta}$. Stage IV dark energy projects such as BigBOSS/MS-DESI, CHIME, Euclid, and SKA can achieve 1% level statistical precision for the velocity measurement through RSD. So once $\eta > 1\%$, the \mathbf{v}_S component becomes non-negligible in RSD modeling. η reaches $\simeq 1\%$ at $k = 0.1h/\text{Mpc}$ and $z \lesssim 1$ (Fig. 4). Even at high redshift $z = 2$, $\eta \simeq 1\%$ at $k = 0.2h/\text{Mpc}$. These results agree with calculation by high-order perturbation theory (Fig. 1, Paper I). It confirms our conclusion in Paper I that, in general \mathbf{v}_S is a non-negligible velocity component, even at scales which are often considered as linear. Its contribution to the redshift space matter power spectrum will be quantitatively studied in future works. Future work will also explore information

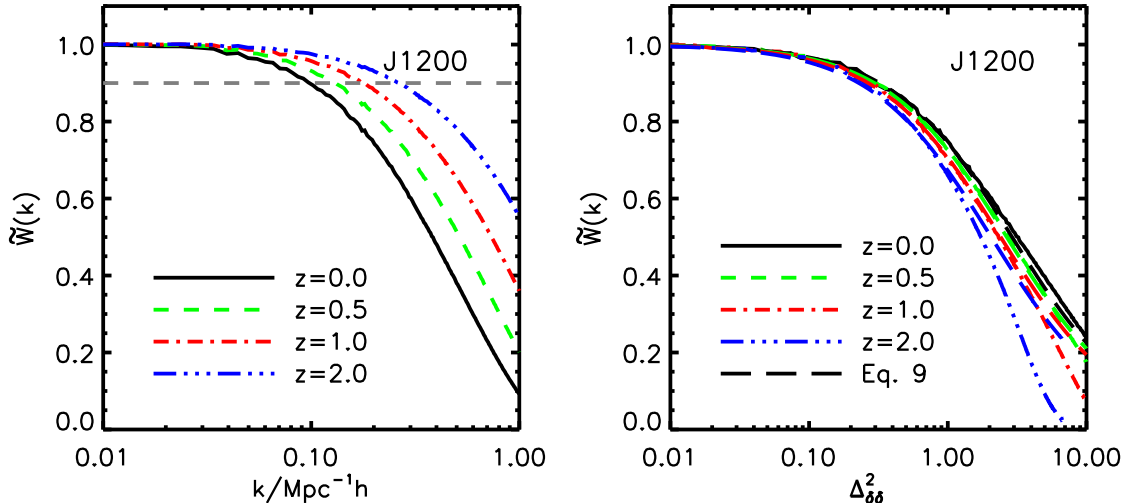


FIG. 5: *Left panel:* the $\tilde{W}(k, z) - k$ relation, calculated from the J1200 simulation. \tilde{W} changes from unity at $k \rightarrow 0$ to zero at $k \rightarrow \infty$. $1 - \tilde{W} \gtrsim 10\%$ at $k = 0.1h/\text{Mpc}$ and $z \lesssim 0.5$, indicating a significant systematic error in RSD cosmology even for stage III dark energy surveys like BOSS and eBOSS. *Right panel:* the $\tilde{W}(k, z) - \Delta_{\delta\delta}^2$ relation. Long dashed lines represent the fitting formula [Eq. (13)] with the best-fit Δ_α listed in Table. II. Comparing to the $\tilde{W}-k$ curves in the left panel, the redshift dependence of $\tilde{W}-\Delta_{\delta\delta}^2$ curves is greatly reduced.

encoded in \mathbf{v}_S . For example, it may be used to probe the environmental dependence of modified gravity theories (Paper I).

Perturbation theory is also useful to understand the redshift evolution of \mathbf{v}_S . From the continuity equation,

$$\dot{\delta} + \nabla \cdot (1 + \delta)\mathbf{v} = 0, \quad (10)$$

the leading-order contribution to \mathbf{v}_S comes from $\dot{\delta}^{(2)}$ and $\delta^{(1)}\mathbf{v}^{(1)}$. Here, $\delta = \sum_i \delta^{(i)}$ is the sum over contributions of i th order density component. To a good approximation, $\delta^{(i)} \propto D^i$ [52]. So both contributions to \mathbf{v}_S evolve as $\propto D^2 f H$. Unlike the case of the density power spectrum, the leading-order contribution to $P_{v_S v_S}$ do not have contribution from third-order components (e.g., $\langle \dot{\delta}^{(3)} v^{(1)} \rangle$) because \mathbf{v}_S vanishes at linear order ($\mathbf{v}_S^{(1)} = 0$). So the perturbation theory predicts that

$$P_{v_S v_S}(z) \propto (D^2 f H)^2. \quad (11)$$

Figures 2 and 3 verify this relation at $k \lesssim 0.1h/\text{Mpc}$. But it quickly loses accuracy toward higher k (smaller scales).

Surprisingly, perturbation theory works much better to understand $\eta \equiv P_{v_S v_S}/P_{v_\delta v_\delta}$. It predicts $\eta \propto D^2$ [Eq. (9) and 11)]. Figure 4 shows that it works even at $k = 0.7h/\text{Mpc}$. Another interesting finding to report is the surprisingly simple scale dependence of $\eta(k, z)$, despite complexities in shapes of both \mathbf{v}_δ and \mathbf{v}_S (Fig. 1). It is well described by a power law. Over the range $k \in (0.01, 1)h/\text{Mpc}$, $\eta(k) \propto k^{n_\eta}$ with $n_\eta \simeq 2.2$ (Fig. 4). Whether these behaviors are coincident or generic

requires further investigation. If these behaviors are generic, they can be utilized to further reduce degrees of freedom in RSD modeling.

\mathbf{v}_B , the curl component, grows only where shell crossing and multistreaming happen. This is the place where perturbation theory, which is based on the single fluid approximation, breaks down. So we lose a powerful tool to understand its behavior. Nevertheless, [51] found that $P_{v_B v_B}(z) \propto D^7(z)$. Our results confirm this relation (Fig. 3). Figure 1 shows that \mathbf{v}_B grows later than \mathbf{v}_S . It is less than 1% of \mathbf{v}_δ at $k = 0.3h/\text{Mpc}$. It is subdominant to \mathbf{v}_S at $k \lesssim 3h/\text{Mpc}$. Our convergence tests presented in the Appendix do not find significant numerical artifacts on \mathbf{v}_B measured from the 100Mpc/h G100 simulation at $k \lesssim 3h/\text{Mpc}$. So the above results should be reliable. We may also expect that the velocity field becomes completely randomized at sufficiently small scales, so $P_{v_B v_B} \rightarrow 2P_{v_S v_S}$. We do find this sign of equipartition at $k \sim 10h/\text{Mpc}$. However, numerical artifacts at these regimes are non-negligible, as shown in the Appendix. Simulations with resolution higher than G100 are required to study this issue.

B. The window function $\tilde{W}(k, z)$

The window function $W(k)$ [Eq. (3)] and the normalized one, $\tilde{W}(k) \equiv W(k)/W(k \rightarrow 0) = W(k)/f$, are of crucial importance for the following reasons in understanding and reconstructing the velocity field and in improving RSD modeling (Paper I). (1) \tilde{W} describes the

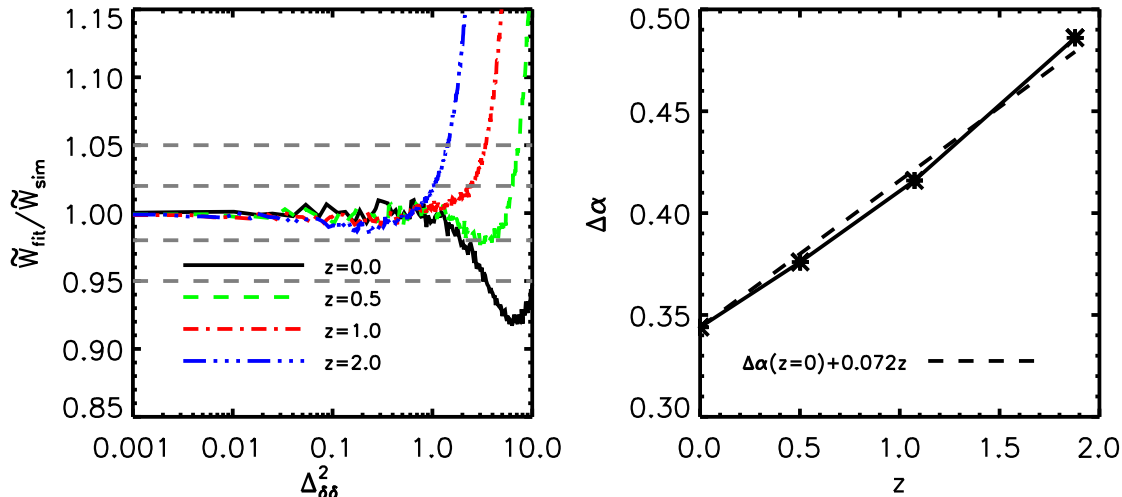


FIG. 6: *Left panel:* $\tilde{W}(k)_{\text{fit}}/\tilde{W}(k)_{\text{sim}}$ with best fitted Δ_α at each redshift. The fitting formula (Eq. 13) achieves an accuracy within 2% at scales of interest for RSD cosmology ($\Delta_{\delta\delta}^2 \leq 1$) at all redshifts. *Right panel* shows the best-fit Δ_α at four redshifts. The redshift dependence in Δ_α is essentially linear relation, with a slope $b \simeq 0.072$ (dashed line).

impact of the nonlinear evolution on the velocity-density relation. (2) \tilde{W} quantifies a major systematic error in RSD cosmology. We have shown that the leading term in the redshift space matter power spectrum $P_{\delta\delta}^s(k, u)$ is $P_{\delta\delta}(1 + f\tilde{W}(k)u^2)^2$. Hence the widely adopted Kaiser formula underestimates f by a factor $\tilde{W}(k) \leq 1$. Perturbation theory predicts a $\sim 10\%$ bias at $k = 0.1h/\text{Mpc}$ and $z = 0$ (Paper I), much larger than the statistical error associated with stage IV dark energy surveys. (3) W behaves as a window function exerting on the density field to reveal the underlying velocity field. This deterministic function can be inferred from RSD in spectroscopic redshift surveys in less model dependent way. So it is essential in three-dimensional peculiar velocity reconstruction in redshift surveys, *at cosmological distances*.

Figure 5 shows $\tilde{W}(k)$ at different redshifts measured in the J1200 simulation. It confirms our theoretical prediction using third-order Eulerian perturbation theory (Paper I), which is applicable at $k \lesssim 0.2h/\text{Mpc}$. As expected, \tilde{W} changes from unity at $k \rightarrow 0$ to zero at $k \rightarrow \infty$. As explained in Paper I, $1 - \tilde{W}$ quantifies a systematic error in f . Since stage IV dark energy surveys have the potential to measure f to $\sim 1\%$ level accuracy, this \tilde{W} -induced systematic error becomes significant, even at relatively high redshift $z = 2$ and pretty linear scale $k = 0.1h/\text{Mpc}$. The situation worsens towards lower redshifts and smaller scales. For example, $1 - \tilde{W} \gtrsim 10\%$ at $z \lesssim 0.5$. It is already significant for stage III dark energy surveys like BOSS and eBOSS [53–55]. This systematic error may contribute a significant fraction to the tension in f between existing measurements and the prediction from Planck cosmology [56].

We expect the degrees of freedom in \tilde{W} is limited. The

perturbation theory predicts [52], for a power law initial power spectrum with power index n ,

$$\begin{aligned} \tilde{W}(k, z) &= \frac{1 + \alpha_{\delta\theta}(n)\Delta_L^2(k, z) + O(\Delta_L^4)}{1 + \alpha_{\delta\delta}(n)\Delta_L^2(k, z) + O(\Delta_L^4)} \quad (12) \\ &\simeq \frac{1}{1 + \Delta_\alpha(n)\Delta_L^2(k, z)}. \end{aligned}$$

Here, Δ_L^2 is the linear matter power spectrum variance and Δ_{NL}^2 is the nonlinear one. The α symbols follow the notation in [52] and $\Delta_\alpha(n) \equiv \alpha_{\delta\delta}(n) - \alpha_{\delta\theta}(n)$. However, in reality, the power index depends on k . So Δ_α is a function of both k and z . In this case n is often approximated as the effective power index at the nonlinear scale k_{NL} , defined through $\Delta_L^2(k_{\text{NL}}, z) = 1$. Even so, $\Delta_\alpha = \Delta_\alpha(n_{\text{eff}}(k_{\text{NL}}(z)))$, a function of redshift. On the other hand, the neglected terms of $O(\Delta_L^4)$ imply a stronger dependence than Δ_L^2 . These considerations motivate us to propose the following fitting formula:

$$\begin{aligned} \tilde{W}(k, z) &= \frac{1}{1 + \Delta_\alpha(z)\Delta_{\text{NL}}^2(k, z)} \quad (13) \\ &\equiv \frac{1}{1 + \Delta_\alpha(z)\Delta_{\delta\delta}^2(k, z)}. \end{aligned}$$

Redshift	Δ_α	χ^2	χ_{dof}^2	N_{data}
$z = 0$	0.344	1.001	0.026	38
$z = 0.5$	0.376	1.0	0.019	54
$z = 1$	0.416	1.001	0.012	82
$z = 2$	0.486	1.01	0.007	145

TABLE II: Fitting parameters. $\chi^2 = \sum (\tilde{W}_{\text{fit}} - \tilde{W}_{\text{sim}})^2$.

Notice that we have replaced the linear matter power spectrum with the nonlinear one. Although we still adopt the symbol $\Delta\alpha$, it is no longer a prediction from perturbation theory. Instead, it shall be treated as a free function to be fitted against simulation or observation. Nevertheless, from the above argument, we do not expect a strong redshift dependence in $\Delta\alpha$.

To check for the above arguments, we plot \tilde{W} against $\Delta_{\delta\delta}^2$ (right panel, Fig. 5). Comparing to the \tilde{W} - k curves in the left panel, we find that the redshift dependence of \tilde{W} - $\Delta_{\delta\delta}^2$ curves is greatly reduced. Curves of different redshifts almost overlap with each other at $\Delta_{\delta\delta}^2 \lesssim 1$. This behavior suggests that \tilde{W} is mainly determined by $\Delta_{\delta\delta}^2$. Impacts of any other factors should be minor.

We then obtain the best-fit value of $\Delta\alpha$ at each redshift. Table II lists the best-fit $\Delta\alpha$, the associated χ^2 and reduced χ^2 . We limit the fitting to $\Delta_{\delta\delta}^2 \leq 1$, where robust cosmology based on RSD is promising. Furthermore, the proposed fitting formula is not expected to work well at $\Delta_{\delta\delta}^2 \gg 1$ (Fig. 6).

It turns out that the proposed fitting formula works excellently at $\Delta_{\delta\delta}^2 < 1$ (Fig. 6). It achieves an accuracy within 2% at scales of interest for RSD cosmology ($\Delta_{\delta\delta}^2 \leq 1$).

The best-fit $\Delta\alpha$ varies weakly with redshift. The redshift dependence can be excellently approximated as linear,

$$\Delta\alpha(z) \simeq \Delta\alpha(z=0) + bz, \quad (14)$$

with $b \simeq 0.072$ (Fig. 6).

By far we have illustrated the possibility of finding a simple fitting formula to accurately model $\tilde{W}(k, z)$. We caution that, although the proposed form [Eq. (13)] works very well, it may not necessarily be the best-fitting formula. What we really want to demonstrate here is that \tilde{W} has very limited degrees of freedom such that one or two fitting parameters are sufficient to model it to high accuracy. This means that we can efficiently reduce the \tilde{W} -induced systematic error without significantly inflating the statistical error in f . Whether we can find a more physically motivated and hence more generic and more accurate fitting formula is an issue for further investigation.

C. The velocity correlation function

RSD modeling in Paper I requires information on the velocity correlation function. The correlation function $\xi_{ij}(\mathbf{r}) \equiv \langle v_i(\mathbf{x}_1)v_j(\mathbf{x}_2) \rangle$ between the i th velocity component at position \mathbf{x}_1 and j th velocity component at $\mathbf{x}_2 = \mathbf{x}_1 + \mathbf{r}$ can be decomposed into two correlation functions ψ_{\perp} and ψ_{\parallel} [4],

$$\xi_{ij}(\mathbf{r}) = \psi_{\perp}(r)\delta_{ij} + [\psi_{\parallel}(r) - \psi_{\perp}(r)] \frac{r_i r_j}{r^2}. \quad (15)$$

Here ψ_{\parallel} is the correlation function of the velocity components along \mathbf{r} and ψ_{\perp} is the one of velocity components

perpendicular to \mathbf{r} . $i = x, y, z$ denote the Cartesian axis. $\mathbf{r} \equiv \mathbf{x}_1 - \mathbf{x}_2$ is the pair separation vector.

ψ_{\parallel} and ψ_{\perp} do not depend on the choice of coordinate system. The two are not independent. For a potential flow (like \mathbf{v}_{δ} and \mathbf{v}_S), we have the textbook result [4],

$$\begin{aligned} \psi_{\parallel}(r) &= \frac{d(r\psi_{\perp}(r))}{dr}, \\ \psi_{\perp}(r) &= H^2 \int \Delta_{\theta\theta}^2 \left[\frac{\sin(kr)}{(kr)^3} - \frac{\cos(kr)}{(kr)^2} \right] \frac{dk}{k^3}. \end{aligned} \quad (16)$$

Paper I derives the relation for a curl velocity field like \mathbf{v}_B ,

$$\begin{aligned} \psi_{\perp}(r) &= \psi_{\parallel}(r) + \frac{1}{2} r \frac{d\psi_{\parallel}(r)}{dr}, \\ \psi_{\parallel}(r) &= \int \Delta_{v_B v_B}^2 \left[\frac{\sin(kr)}{(kr)^3} - \frac{\cos(kr)}{(kr)^2} \right] \frac{dk}{k}. \end{aligned} \quad (17)$$

What is relevant for RSD modeling is $\xi_{v_z v_z}(\mathbf{r})$, assuming the line of sight as the z axis. One can easily verify that

$$\begin{aligned} \xi_{v_z v_z}(\mathbf{r} = (0, 0, r)) &= \psi_{\parallel}(r), \\ \xi_{v_z v_z}(\mathbf{r} = \mathbf{r}_{\perp}) &= \psi_{\perp}(r). \end{aligned} \quad (18)$$

One can also prove that

$$\xi_{v_z v_z}(r) \equiv \langle \xi_{v_z v_z}(\mathbf{r}) \rangle_{\mathbf{r}} = \frac{1}{3} (\psi_{\parallel}(r) + 2\psi_{\perp}(r)). \quad (19)$$

Figure 7 shows the simulated $\xi_{v_z v_z}(r)$ (left column), $\psi_{\parallel}(r)$ (middle column) and $\psi_{\perp}(r)$ (right column). It also verifies the above relation (dashed lines in left column). Equations (16) and (17) are also verified against their integral forms [Eq. (16) by dot-dashed lines in right column, Eq. (17) by dotted lines in middle column]:

$$\begin{aligned} r\psi_{\parallel,B} &= \int_0^r (2\psi_{\perp,B} - \psi_{\parallel,B}) dr, \\ r\psi_{\perp,S,\delta} &= \int_0^r \psi_{\parallel,S,\delta} dr. \end{aligned}$$

There are slight deviations in the comparison, likely caused by the simplest trapezoidal rule for integration, or sparse sampling in low- k region.

Figure 7 verifies our speculation in Paper I on the correlation lengths of the three velocity components. We see that \mathbf{v}_{δ} has the largest correlation length of $O(100)$ Mpc, in concordance with the fact that its power spectrum peaks at $k \sim 0.05h/\text{Mpc}$. Due to this large correlation length and due to its complete correlation with the density field, its contribution to the redshift space matter power spectrum is the most complicated to model. We refer readers to Paper I for details.

On the contrary, \mathbf{v}_B has the smallest $O(1)$ Mpc correlation length, which is shorter than scales of interest for RSD cosmology. This motivates us to treat it as an uncorrelated field in our RSD modeling [Eq. (21), paper I]. Its impact on RSD is completely captured by the

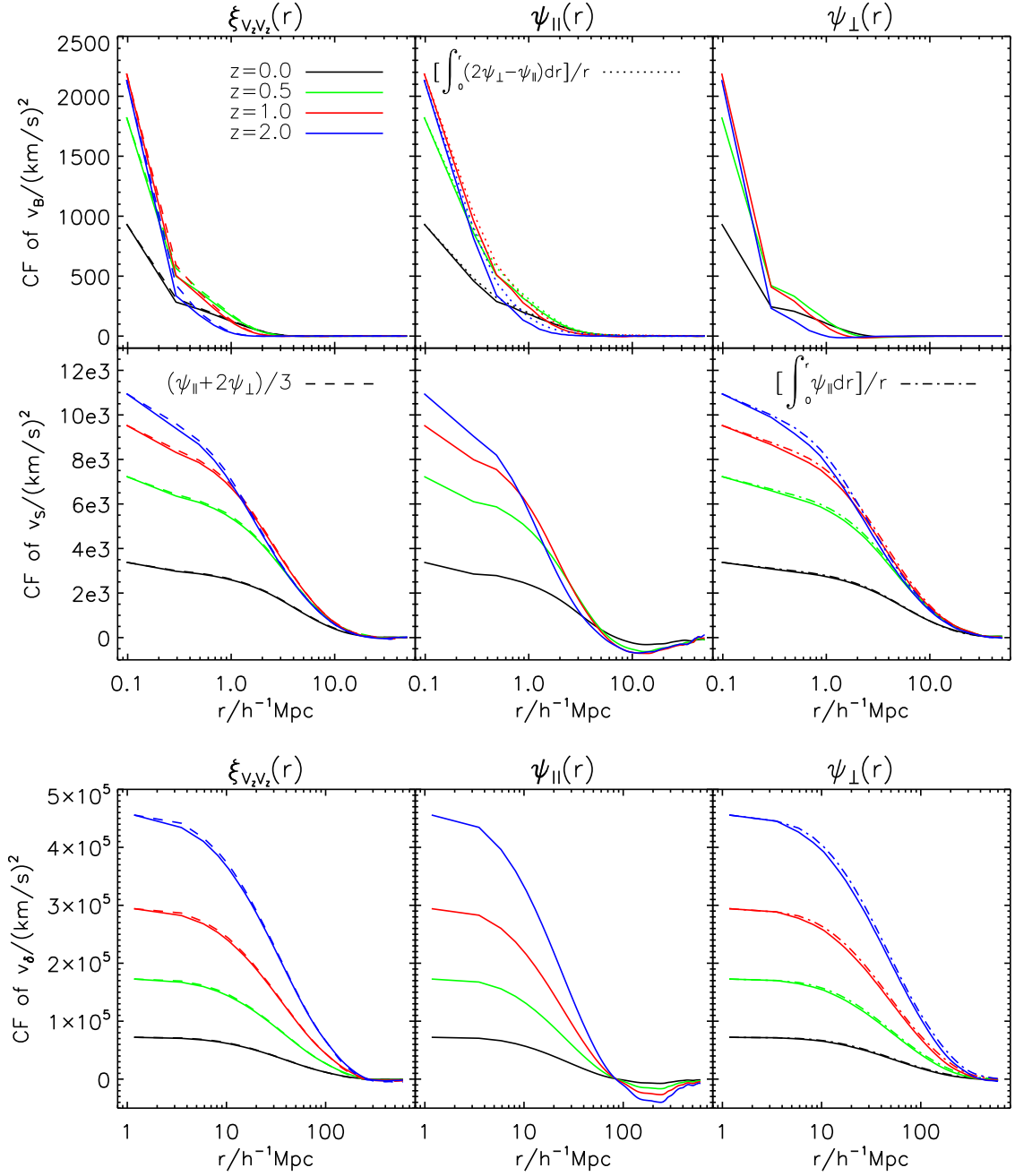


FIG. 7: Three types of correlation function (CF) are shown by solid lines in different columns. Different line colors represent different redshifts. CFs of \mathbf{v}_S are calculated from the J1200 simulation. CFs of $\mathbf{v}_{S,B}$ are calculated from the G100 simulation. They are calculated by Fourier transforming the velocity power spectra. \mathbf{v}_α has the largest $O(100)$ Mpc correlation length. \mathbf{v}_S has a correlation length of $O(10)$ Mpc. \mathbf{v}_B has the smallest $O(1)$ Mpc correlation length. The data point on the left end of each line is actually $\xi_{v_z, \alpha v_z, \alpha}(r=0) = \sigma_{v_\alpha}^2$. *Left panel:* $\xi_{v_z v_z}(r) \equiv \langle \xi_{v_z v_z}(\mathbf{r}) \rangle_{\mathbf{r}}$. The dashed lines are calculated by Eq. (19) and verify this relation. *Middle panel:* $\psi_{||}(r)$ is the correlation function when both velocities are along \mathbf{r} . The dotted lines verify Eq. (17). *Right panel:* $\psi_{\perp}(r)$ is the correlation function when both velocities are perpendicular to \mathbf{r} . The dot-dashed lines verify Eq. (16).

damping function D_B^{FOG} , which will be quantified later in this paper.

Since a significant fraction of \mathbf{v}_S comes from bulk motion, \mathbf{v}_S has a correlation length of $O(10)$ Mpc, larger than that of \mathbf{v}_B . So we have to take into account its

self-clustering [e.g., Eq. (25) of paper I].

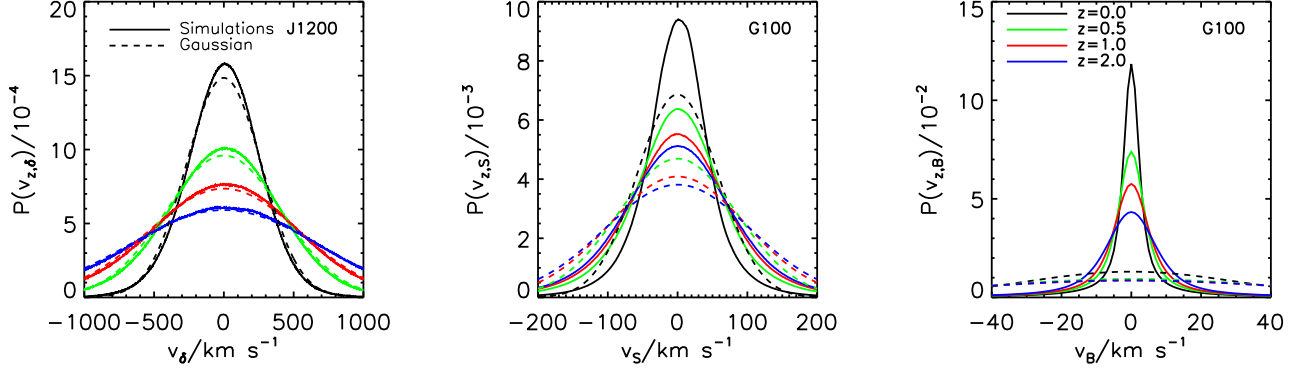


FIG. 8: The PDFs of $\mathbf{v}_{\delta,S,B}$ along the z axis are shown by solid lines. The dashed lines show Gaussian distributions with the same velocity mean and dispersion of corresponding velocity PDFs. Different line colors represent different redshifts. Apparently, \mathbf{v}_{δ} is the most Gaussian velocity component since it mainly correlates with linear matter density field and the window function \tilde{W} suppresses non-Gaussianities from small scales. In contrast, \mathbf{v}_B is strongly non-Gaussian, consistent with the fact that most contribution comes from strongly nonlinear and non-Gaussian scales.

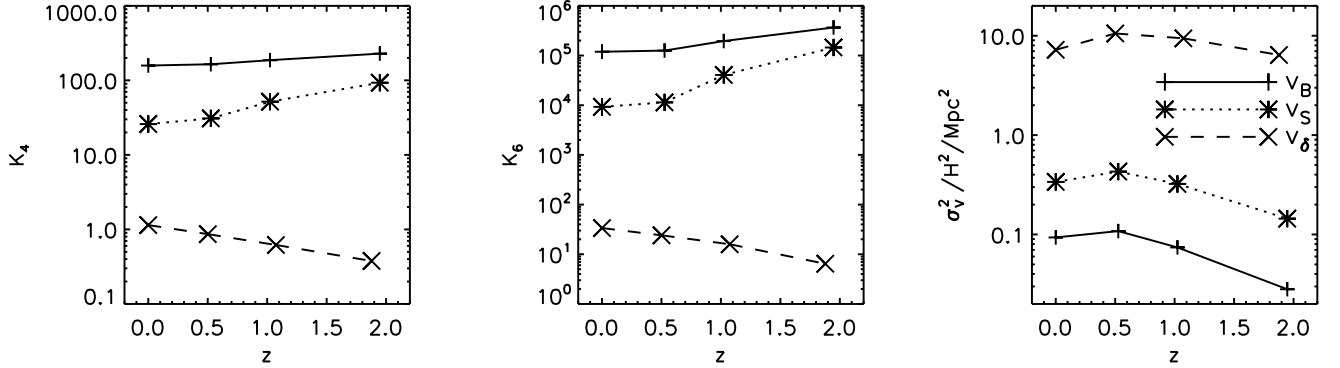


FIG. 9: *Left and middle panels:* The fourth and sixth order of reduced cumulants of $\mathbf{v}_{\delta,S,B}$. They confirm the non-Gaussianity results shown in Fig. 8. Towards lower redshift, non-Gaussianities of $\mathbf{v}_{S,B}$ decrease, likely due to ongoing halo virialization and the associated velocity randomization, while non-Gaussianity of \mathbf{v}_{δ} increases due to nonlinear structure evolution. *Right panel:* σ_v^2/H^2 determines the leading-order damping to redshift space clustering caused by the FOG effect [Eq. (23), Fig. 10].

D. The one-point velocity PDF and cumulants

RSD modeling requires us to quantify the non-Gaussianity of the three velocity components (Paper I). Fig. 8 shows $P(v_{z,\alpha})$ ($\alpha = \delta, S, B$) at different redshifts. For comparison, we also overplot the Gaussian distribution with the same velocity mean (zero) and dispersion. Here, $P(v_{z,\alpha})$ is the corresponding PDF of the velocity component \mathbf{v}_{α} along the z -axis.

To better quantify the non-Gaussianity, we calculate the reduced cumulants of the three velocity components, K_n . The calculation is done against the real space velocity components on regular grid points. The real space velocity components are obtained by Inverse Fourier Transforming the Fourier space velocity components on regular grid points. Since the velocity field is symmetrical,

$\langle v^{2j+1} \rangle_c = 0$. The nonvanishing cumulants are

$$K_4 \equiv \frac{\langle v^4 \rangle}{\langle v^2 \rangle^2} - 3,$$

$$K_6 \equiv \frac{\langle v^6 \rangle}{\langle v^2 \rangle^3} - 10 \frac{\langle v^3 \rangle^2}{\langle v^2 \rangle^3} - 15 \frac{\langle v^4 \rangle}{\langle v^2 \rangle^2} + 30, \dots$$

For Gaussian fields, $K_{n \geq 3} = 0$. But all three velocity components have visible non-Gaussianity (Fig. 9).

\mathbf{v}_{δ} is nearly Gaussian, with $K_4 \lesssim 1$ at all redshifts. This is consistent with the fact that the dominant contribution comes from linear scales (Fig. 1). However, it may appear to contradict the fact that it is completely correlated with the density field, which is highly nonlinear and non-Gaussian. The reason is that $\tilde{W} \ll 1$ at highly nonlinear scales, and hence it filters away most non-Gaussian contribution.

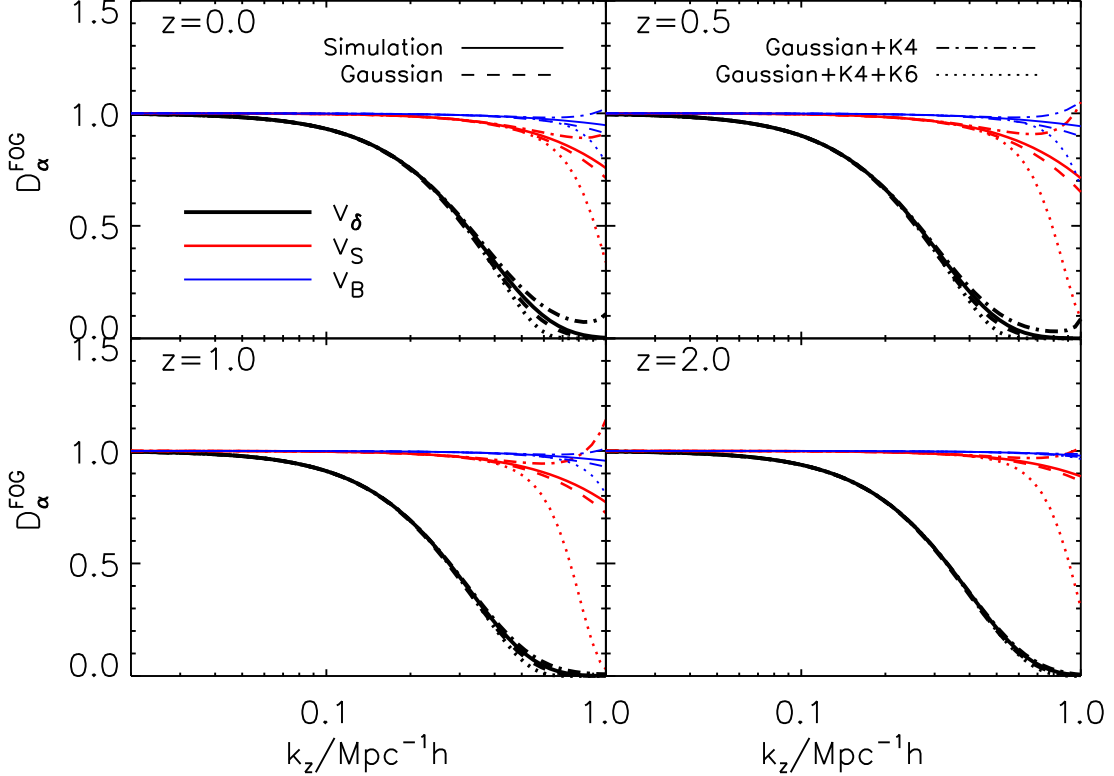


FIG. 10: The damping functions D_α^{FOG} . They quantify the FOG effect of corresponding velocity components. The solid lines are calculated by Eq. (20) through simulations. The other lines are approximations with/without K_4 and/or K_6 terms in Eq. (21). The thick, intermediate thick, and thin lines with different colors represent results of D_δ^{FOG} , D_S^{FOG} and D_B^{FOG} respectively. Apparently \mathbf{v}_δ contributes most to the FOG effect since it has the largest velocity dispersion (right panel of Fig. 9). The model tends to be more accurate towards higher redshift where nonlinearity/non-Gaussianity of matter/velocity field are smaller. The ratios between approximations and simulation calculations are shown in Fig. 11.

In contrast, \mathbf{v}_B is strongly non-Gaussian (Fig. 9), consistent with the fact that most of its contribution comes from strongly nonlinear and non-Gaussian scales. This result also supports our conclusion that the aliasing effect is subdominant in \mathbf{v}_B measured from the G100 simulation, otherwise we may expect a close-to-Gaussian \mathbf{v}_B .

The non-Gaussianity of \mathbf{v}_S falls somewhere between, with visible departure from Gaussianity in the PDF, $K_4 > 10$ and $K_6 > 10^4$.

An interesting behavior is that, $K_{4,6}$ of \mathbf{v}_δ increase towards lower redshift, while $K_{4,6}$ of \mathbf{v}_S and \mathbf{v}_B decrease (Fig. 9). The increase of non-Gaussianity in \mathbf{v}_δ indicates that more and more ‘‘Gaussian’’ scales have been converted to be ‘‘non-Gaussian’’ due to the ongoing non-linear evolution. On the other hand, ongoing virialization in halos and the associated velocity randomization may be responsible for decreasing non-Gaussianity in \mathbf{v}_S and \mathbf{v}_B .

E. The damping functions

Paper I proves that all three velocity components contribute to the FOG effect. Their contributions are described by the corresponding damping function D_α^{FOG} (Paper I),

$$\begin{aligned} \sqrt{D_\alpha^{\text{FOG}}(k_z)} &\equiv \left| \left\langle \exp\left(i\frac{k_z v_{z,\alpha}}{H}\right) \right\rangle \right| & (20) \\ &= \int_{-\infty}^{\infty} \exp\left(i\frac{k_z v_{z,\alpha}}{H}\right) P(v_{z,\alpha}) dv_{z,\alpha} \\ &= \int_{-\infty}^{\infty} \cos\left(\frac{k_z v_{z,\alpha}}{H}\right) P(v_{z,\alpha}) dv_{z,\alpha}. \end{aligned}$$

The cumulant expansion theorem allows us to express D_α^{FOG} in terms of cumulants (Paper I),

$$\sqrt{D_\alpha^{\text{FOG}}(k_z)} = \exp\left(-\frac{x}{2} \left[1 - \frac{K_4}{12}x + \frac{K_6}{360}x^2 + \dots\right]\right), \quad (21)$$

where $x \equiv (k_z \sigma_{v_\alpha}/H)^2$. σ_{v_α} is the one-dimensional ve-

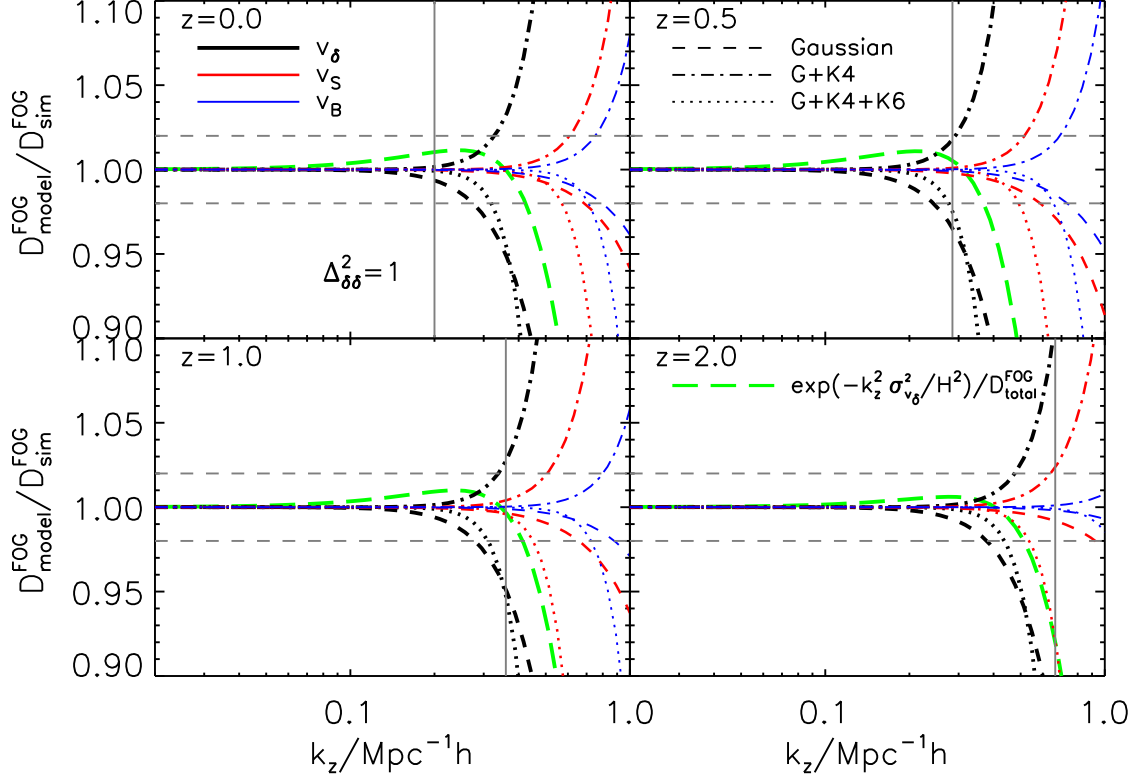


FIG. 11: The accuracy of various approximations of damping functions D_α^{FOG} . The dashed lines show that of the Gaussian approximation [Eq. (23)]. The dot-dashed and dotted lines show that of approximation with K_4 and K_4+K_6 terms respectively. The thick, intermediate thick, and thin lines with different colors correspond to D_δ^{FOG} , D_S^{FOG} , and D_B^{FOG} respectively. The vertical gray lines denote the scale where $\Delta_{\delta\delta}^2(k, z) = 1$. In particular, the thick green dashed lines verify that the approximation Eq. (24) is accurate at $\sim 1\%$ level at $k < 0.3h/\text{Mpc}$.

locity dispersion,

$$\sigma_{v_\alpha}^2 = \xi_{v_{z,\alpha}v_{z,\alpha}}(r=0) = \frac{1}{3} \int \Delta_{v_\alpha v_\alpha}^2(k) \frac{dk}{k}. \quad (22)$$

To the first order, the damping functions take Gaussian form,

$$\sqrt{D_\alpha^{\text{FOG}}(k_z)} = \exp\left(-\frac{x}{2}\right) = \exp\left(-\frac{(k_z \sigma_{v_\alpha})^2}{2H^2}\right). \quad (23)$$

It is completely determined by σ_{v_α}/H (right panel, Fig. 9).

We test the accuracy of Eq. (23) against the exact D_α^{FOG} , calculated from simulations using Eq. (20). Figures 10 and 11 show that Eq. (23) agrees well with the simulation for all three velocity components, for a wide range of k . The accuracy is better than 10% where $\Delta_{\delta\delta}^2 \lesssim 1$.

Can adding higher-order terms such as K_4 and K_6 in Eq. (21) improve the modeling accuracy of D_α^{FOG} ? This test is shown in Fig. 10 and Fig. 11. Unfortunately, including K_4 or $K_4 + K_6$ does not necessarily improve the modeling accuracy of D_α^{FOG} . Instead, including these terms often causes unphysical behaviors such as $D_\alpha^{\text{FOG}} > 1$.

We thus conclude that the Gaussian approximation [Eq. (23)] is in practice the optimal approximation of $D_\alpha^{\text{FOG}}(k_z)$, for all three velocity components. Furthermore, since $\sigma_{v_\delta}^2 \gtrsim 10(\sigma_{v_S}^2 + \sigma_{v_B}^2)$, to high accuracy we can approximate the overall damping function as

$$\begin{aligned} D^{\text{FOG}}(k_z) &\equiv D_\delta^{\text{FOG}}(k_z) D_S^{\text{FOG}}(k_z) D_B^{\text{FOG}}(k_z) \quad (24) \\ &\simeq \exp\left(-\frac{k_z^2(\sigma_{v_\delta}^2 + \sigma_{v_S}^2 + \sigma_{v_B}^2)}{H^2}\right) \\ &\simeq \exp\left(-\frac{k_z^2 \sigma_{v_\delta}^2}{H^2}\right). \end{aligned}$$

Figure 11 verifies that the last approximation works at $\sim 1\%$ accuracy at $k < 0.3h/\text{Mpc}$ and $z \in (0, 2)$.

The excellent performance of the above Gaussian approximation is very surprising, since much of the literature prefers a Lorentz form $D^{\text{FOG}} = 1/(1 + k_z^2 \sigma_v^2 / H^2)$ (e.g. [6, 57–59]) or more complicated ones (e.g. [60]). This seems to contradict our findings. The point is that many of these studies infer the damping function by fitting the form $P_{\delta\delta}^s(k, u) = P_{\delta\delta}(k)(1 + fu^2)^2 D^{\text{FOG}}(ku)$ against simulations. However, there are ignored high-order corrections inside of the parentheses [refer to Eq. (1); For more details, refer to Paper I]. Ignoring these

corrections leads to misinterpretation of FOG. For example, positive high-order corrections can be misinterpreted as a damping function weaker than the Gaussian form. This issue will be further clarified when we quantify the accuracy of the above RSD modeling with simulations.

V. SUMMARIES AND DISCUSSIONS

Numerical results presented in the current paper confirm many of our qualitative arguments and speculations in Paper I. (1) They show that \mathbf{v}_δ dominates over \mathbf{v}_S and \mathbf{v}_B at $k < 0.5h/\text{Mpc}$. The \mathbf{v}_δ field is close to Gaussian, with a correlation length of $O(100)$ Mpc. \mathbf{v}_δ has the largest velocity one-dimension dispersion, $\sigma_{v_\delta} \simeq 270$ km/s at $z = 0$. It not only dominates the large-scale enhancement of redshift space clustering, but also dominates the FOG effect. We also measure a key function \tilde{W} and confirm that it can indeed induce $O(10)\%$ underestimation in f . We show by an example that \tilde{W} has very limited degrees of freedom and can be described by a simple fitting formula accurately. (2) The \mathbf{v}_B field is subdominant at $k < 1h/\text{Mpc}$ and is negligible at $k < 0.5h/\text{Mpc}$. It has the smallest velocity dispersion. Due to observed numerical artifacts, we can only obtain the upper limit $\sigma_{v_B} \leq 30$ km/s ($z = 0$). Furthermore, it has the shortest correlation length and can be treated as a random field. Its impact on RSD is fully captured by the damping function $D_B^{\text{FOG}}(k_z)$. \mathbf{v}_B is highly non-Gaussian. However, due to its small amplitude, $D_B^{\text{FOG}}(k_z)$ is well approximated by a Gaussian form at scales of interest. (3) The \mathbf{v}_S component is sub-dominant, but non-negligible, at $k < 0.5h/\text{Mpc}$. $\sigma_{v_S} \simeq 60$ km/s at $z = 0$. Its correlation length is of $O(10)$ Mpc, so we have to take its clustering into RSD modeling.

There are still many open issues regarding the velocity statistics. Some of them will be addressed in our future works. We just list a few of them here. One immediate question is the halo velocity field. Once we understand it, we can understand the galaxy velocity field with the help of halo model. This piece of information is essential to model the galaxy RSD. Another issue is cosmological dependences of these velocity statistics. An associated question is the information budget in each velocity component, as a function of redshift and scale.

VI. ACKNOWLEDGEMENTS

We thank Jiawei Shao and Yu Yu for useful discussions. This work was supported by the National Science Foundation of China (Grants No. 11025316, No. 11121062, No. 10873035, No. 1133003, No. 10873027, No. 11121062, and No. 11233005), the National Basic Research Program of China (973 Program) under Grant No. 2009CB24901 and the CAS/SAFEA International Partnership Program for Creative Research Teams

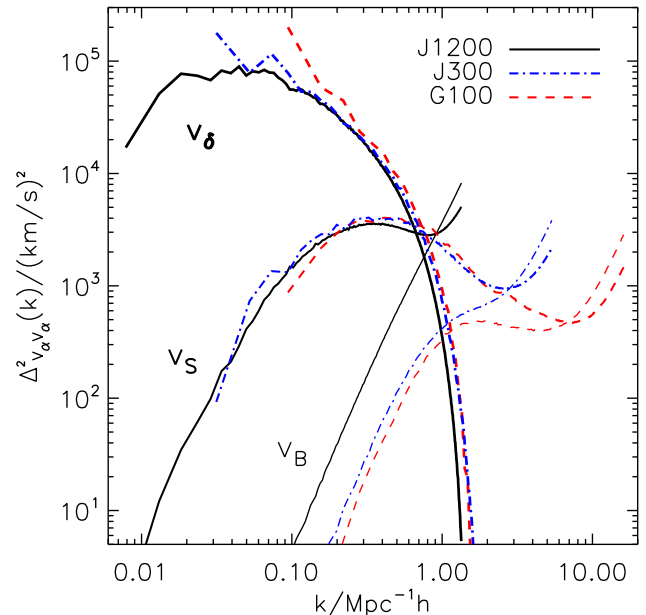


FIG. 12: Comparison between the three simulations at $z = 0$. The velocity power spectra $\Delta_{v_\alpha}^2(k)$ ($\alpha = \delta, S, B$) are calculated with $N_{\text{grid}} = 512^3$. (1) \mathbf{v}_δ in J1200 loses power at $k \gtrsim 0.3h/\text{Mpc}$ due to its low resolution, while \mathbf{v}_δ in G100 suffers from large cosmic variance at $k \lesssim 0.3h/\text{Mpc}$. Combining the \mathbf{v}_δ measurement of J1200 at $k \lesssim 0.3h/\text{Mpc}$ and G100 at $k \gtrsim 0.3h/\text{Mpc}$ thus provides reliable determination of the \mathbf{v}_δ field. Combining the J300 simulation at $k \sim 0.3h/\text{Mpc}$ can be more reliable, although we have not done so in this paper. (2) The spurious increase of \mathbf{v}_S at $k \sim 0.8h/\text{Mpc}$ ($k \sim 2h/\text{Mpc}$) measured by J1200 (J300) is caused by numerical artifacts. (3) Both J1200 and J300 fail to simulate \mathbf{v}_B at any scales.

(KJCX2-YW-T23).

Appendix A: Testing the NP method

The NP (Nearest-Particle) method we proposed is simple and straightforward to implement. Despite its simplicity, we argue that it is robust in a number of ways and is hence sufficiently accurate for the statistics presented in this paper. We will run a number of convergence tests to demonstrate its robustness. We will also quantify its accuracy for a number of fiducial velocity fields, which resemble realistic velocity fields.

1. The convergence tests

The convergence tests we consider are as follows: (1) Convergence between the three simulations. J1200, J300 and G100 all have 1024^3 particles, but have different box sizes and mass resolutions. By comparing the three sim-

ulations, we can estimate the reliable range of the simulated velocity field. (2) Convergence against the grid size. We assign properties of simulation particles to regular grids in order to do Fast Fourier transformation (FFT). The price to pay is that information at subgrid scales is smoothed out. Furthermore, as an approximated way of sampling the velocity field, it can cause misidentification of different velocity components. For example, finite grids are known to cause spurious \mathbf{v}_B [51]. By varying the grid number and checking for the convergence, we can figure out suitable grid choices and a reliable range of the measured velocity statistics. (3) *Sampling bias*. The issues addressed in (1) and (2) can be regarded as sampling biases. But throughout the paper we refer to the sampling bias as that caused by the fact that we only have velocity where there are particles. By sampling the velocity field using only a fraction of particles, we amplify this sampling bias. Observing its dependence with respect to the fraction of particles, we can estimate this sampling bias. In particular, if the measured velocity statistics converge when the used fraction of particles is above a certain value, we will have reasonable confidence on the velocity statistics using all particles.

We only show test results at $z = 0$, where numerical artifacts are the most severe. Furthermore, we mainly test the convergence in the power spectrum. The convergence tests can be extended to other statistics.

a. Comparison between the three simulations

Simulation box size determines the lower limit of reliable range of k , while mass resolution determines the upper limit of reliable range of k .

Figure 12 plots $\Delta_{v_\alpha v_\alpha}^2$ ($\alpha = \delta, S, B$) calculated respectively from J1200, J300 and G100. It shows various spurious behaviors and various discrepancies between these simulations. These are manifests of numerical artifacts. In particular, $\Delta_{v_B v_B}^2$ decreases rapidly with increasing resolution from J1200 to G100. This is consistent with the finding in [51]. Further tests, especially that in Sec. A2, will identify the origin of this numerical artifact. Figure 12 implies by naive scaling that, simulations of Gpc box size and 10^{12} particles are needed to fully control these numerical artifacts. Although a daunting task, such simulation is within the capability of state of art computation.

Nevertheless, J1200/J300/G100 do converge here and there, where we expect the simulation results to be reliable. Figure 12 (and figures hereafter) implies that, combining these simulations, it is feasible to reliably measure the power spectrum of the three velocity fields in the range of interest ($k \in [0.01, 1]h/\text{Mpc}$). In this paper, we combine J1200 at $k < 0.3h/\text{Mpc}$ and G100 at $k > 0.3h/\text{Mpc}$ to measure $\Delta_{v_\delta v_\delta}^2$ and $\Delta_{v_S v_S}^2$. We use G100 to calculate $\Delta_{v_B v_B}^2$.

For other statistics such as the one-point PDFs, cumulants, and the damping functions, different scales mix

and we have difficulty combining these simulations. To address this, we take a simplified approach. Since the power of \mathbf{v}_δ peaks at $k \lesssim 0.1h/\text{Mpc}$ where J1200 is the most reliable, we only use J1200 to measure statistics of \mathbf{v}_δ . Both the power of \mathbf{v}_S and \mathbf{v}_B peak at $k \gtrsim 0.3h/\text{Mpc}$ where G100 is most reliable, so we use G100 to measure statistics of $\mathbf{v}_{S,B}$.

b. Grid size

We calculate the power spectrum by assigning particle properties (mass, velocity, etc.) onto regular grid points and performing FFT. A natural convergence test is then against the grid size L_{grid} . Figure 13 shows $\Delta_{v_\alpha v_\alpha}^2$ ($\alpha = \delta, S, B$) calculated in the J1200 and G100 simulations respectively, with $N_{\text{grid}} = 256^3, 512^3, 1024^3$. (1) Convergence tests with J1200 show that grid-size-associated numerical artifacts in \mathbf{v}_δ are negligible at $k \lesssim 0.3h/\text{Mpc}$, for grid size $L_{\text{grid}} = 4.7h^{-1}\text{Mpc}$ ($N_{\text{grid}} = 256^3$). They are negligible at $k \lesssim 1h/\text{Mpc}$, for grid size $L_{\text{grid}} = 2.3h^{-1}\text{Mpc}$ ($N_{\text{grid}} = 512^3$). Convergence tests with G100 show that numerical artifacts in \mathbf{v}_δ associated with grid size are negligible at $k \lesssim 1h/\text{Mpc}$, for grid size $L_{\text{grid}} < 0.4h^{-1}\text{Mpc}$ ($N_{\text{grid}} = 256^3$). (2) J1200 and G100 show that grid-size-associated numerical artifacts in \mathbf{v}_S are negligible at $k \times \text{Mpc}/h \lesssim 0.1$ (0.3, 1, 2), for $L_{\text{grid}}/h^{-1}\text{Mpc} = 4.7$ (2.3, 0.4, 0.2). (3) Convergence tests with G100 show that, to reliably measure \mathbf{v}_B to $k = 1h/\text{Mpc}$, grid size $L_{\text{grid}} \leq 0.4h/\text{Mpc}$ is required. To reach $k = 2h/\text{Mpc}$, $L_{\text{grid}} \leq 0.2h/\text{Mpc}$ is required. We are then able to conclude that, the measured power spectra shown in Fig. 1 are robust against numerical artifacts associated with nonzero grid size (finite grid number).

Nonetheless, we do find significant disagreement between different grid sizes over some k ranges in Fig. 13. These are clear manifestation of significant numerical artifacts associated with grid size. The situation is the most severe for \mathbf{v}_B . No convergence is found in J1200, meaning that even with $L_{\text{grid}} = 1.2h^{-1}\text{Mpc}$, it is not sufficient to accurately sample the \mathbf{v}_B field. Tests with G100 show that $L_{\text{grid}} \lesssim 0.4h^{-1}\text{Mpc}$ is needed to accurately measure \mathbf{v}_B at $k \lesssim 1h/\text{Mpc}$.

There are at least three types of numerical artifacts associated with grid size: (1) One is the smoothing effect, suppression of small-scale power caused by the assignment window function (e.g., [61] and references therein). (2) Another is the alias effect caused by finite grid number. It causes mixture of power among wave vectors $\mathbf{k} + 2k_N\mathbf{n}$ [61]. Here $k_N \equiv \pi/L_{\text{grid}}$ is the Nyquist wave number and L_{grid} is the grid size. \mathbf{n} is the three-dimensional integer vector. These two biases also exist for the matter power spectrum measurement. (3) For the velocity measurement, there is another type of alias effect. It causes mixture between different velocity components [51]. This effect is especially severe for \mathbf{v}_B measurement.

All three types of bias depend on the grid size (num-

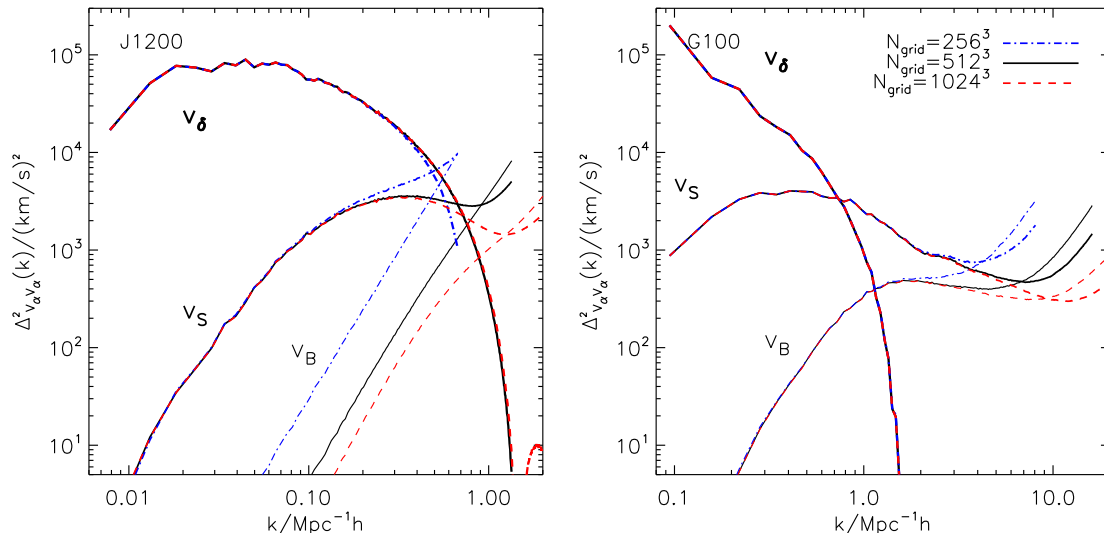


FIG. 13: Convergence tests on the grid size, for J1200 (left panel) and G100 (right panel) respectively. Fine grids are required to robustly sample the velocity and density field. For a given grid size, we should only trust the regimes where the result agrees with that of finer grids. Our tests show that 512^3 grid of J1200 are needed to measure \mathbf{v}_δ and \mathbf{v}_S at $k \lesssim 0.3h/\text{Mpc}$. Going to smaller scales should resort to the G100 simulation. 512^3 grids of G100 are needed to measure \mathbf{v}_B at $k \lesssim 1h/\text{Mpc}$.

ber). The assignment window function for the NP method is $W_a(\mathbf{r}, \mathbf{r}_g) = \delta^D(\mathbf{r} - \mathbf{r}_{NP}(\mathbf{r}_g))$. Here \mathbf{r}_g is the position of the given grid point and $\mathbf{r}_{NP}(\mathbf{r}_g)$ is the location of the corresponding nearest particle. Notice that this window function is inhomogeneous. Namely, it is not completely determined by $\mathbf{r} - \mathbf{r}_g$. So the formula of alias effect, derived with the condition $W_a(\mathbf{r}, \mathbf{r}_g) = W_a(\mathbf{r} - \mathbf{r}_g)$ in [61], does not apply here. It is beyond the scope of this paper to derive a general expression of the alias effect. Instead, we work on a limiting case of infinite particle number density ($N_P/L_{\text{box}}^3 \rightarrow \infty$). Under this limit, $\mathbf{r}_{NP}(\mathbf{r}_g) \rightarrow \mathbf{r}_g$ and $W_a(\mathbf{r}, \mathbf{r}_g) \rightarrow \delta^D(\mathbf{r} - \mathbf{r}_g)$. Following [61], we obtain

$$P_{\mathbf{v}\mathbf{v}}^f(\mathbf{k}) \rightarrow \sum_{\mathbf{n}} P_{\mathbf{v}\mathbf{v}}(\mathbf{k} + 2k_N\mathbf{n}). \quad (\text{A1})$$

Under this limit, the smoothing effect vanishes (the prefactor of the power spectrum at $\mathbf{n} = (0, 0, 0)$ is unity). The alias effect, on one hand, shows as contaminations from $\mathbf{k} + 2k_N\mathbf{n}$ modes with $\mathbf{n} \neq (0, 0, 0)$ to the measure \mathbf{k} mode. On the other hand, it shows as leakages between different velocity components ($\mathbf{v}_\delta \rightarrow \mathbf{v}_S$, $\mathbf{v}_\delta \rightarrow \mathbf{v}_B$, $\mathbf{v}_S \leftrightarrow \mathbf{v}_B$). Sec. A2 will quantify these leakages. Both alias effects contribute to the decreasing of power at small scales in both \mathbf{v}_S and \mathbf{v}_B (Fig. 13).

These convergence tests show that, by combining J1200/J300/G100 we can safely neglect the smoothing and aliasing caused by nonzero grid size at scale of interest. So we do not attempt to correct for these numerical artifacts. For methods of correcting them, refer to [51, 61–63].

c. Sampling bias

To highlight the sampling bias, we randomly select 50%, 25%, and 10% of the simulation particles and compare the measured velocity power spectra with those of 100% particles (Fig. 14). A complexity is that, the assignment window function of the NP method $W_a(\mathbf{r}, \mathbf{r}_g)$ is particle number density dependent. So reducing the number of particles sampled also changes the alias effect. Hence the numerical artifacts shown in Fig. 14 should be a mixture of sampling bias and alias effect. We do not attempt to separate the two in this paper.

For J1200, the power spectra of \mathbf{v}_δ and \mathbf{v}_S converge at $k \lesssim 0.2h/\text{Mpc}$. At $k = 0.3h/\text{Mpc}$, the results vary between the four cases (10%, 25%, 50%, and 100%). We then know that $1024^3 \times 50\%$ particles are not sufficient to simulate \mathbf{v}_δ and \mathbf{v}_S at $k \approx 0.3h/\text{Mpc}$. However, we do not know if 1024^3 particles are sufficient. The situation for \mathbf{v}_B is much worse. The power of \mathbf{v}_B decreases with increasing number density at all scales. This again confirms that the measured \mathbf{v}_B in J1200 is mainly numerical artifact, instead of real signal.

For G100, convergences are much better, since the sampling bias should decrease rapidly towards higher particle number density. These convergences tell us that sampling bias in a G100 like simulation with 1024^3 particles and $100h^{-1}/\text{Mpc}$ box is negligible at $k \lesssim 1h/\text{Mpc}$ for all the three velocity components.

Figure 15 shows correlation functions under the same conditions. It shows that the NP method gives considerably accurate estimations for $\sigma_{v_\delta}^2$ and $\sigma_{v_S}^2$, but overestimates $\sigma_{v_B}^2$. This is consistent with the large discrepancies

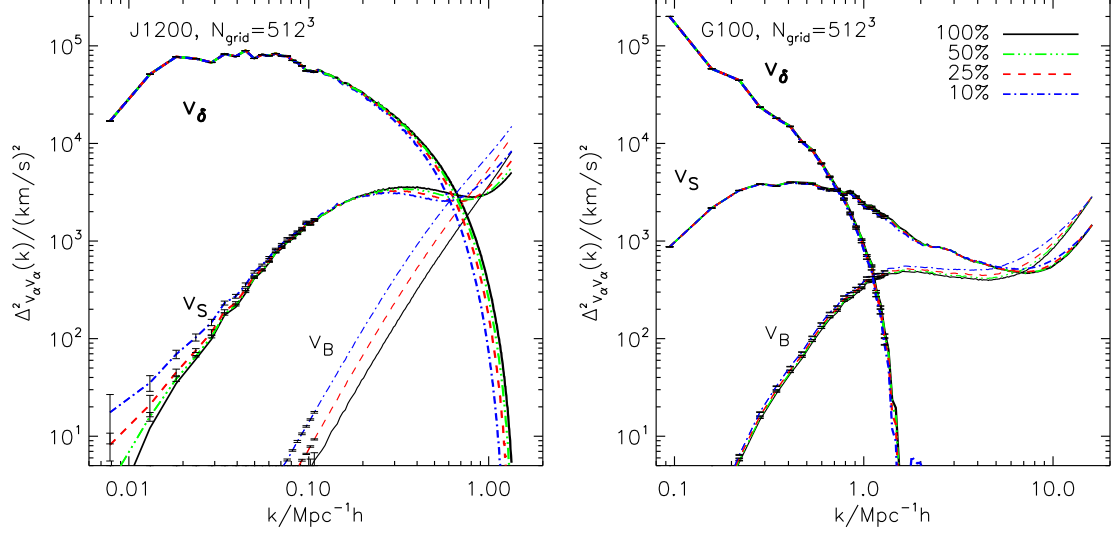


FIG. 14: $\Delta_{v_\alpha v_\alpha}^2$ ($\alpha = \delta, S, B$) of J1200 (left panel) and G100 (right panel) calculated using a fraction of randomly selected particles. This test quantifies the sampling bias. The error bars are calculated by ten realizations of randomly selected 50% and 25% particles, and 20 realizations of 10% particles. For clarity, not all error bars are shown. Test on J1200 finds visible sampling bias at $k \gtrsim 0.3h/\text{Mpc}$ in \mathbf{v}_δ and \mathbf{v}_S . It also tells us that \mathbf{v}_B measured by J1200 is mainly noise. On the other hand, test on G100 shows much better convergence.

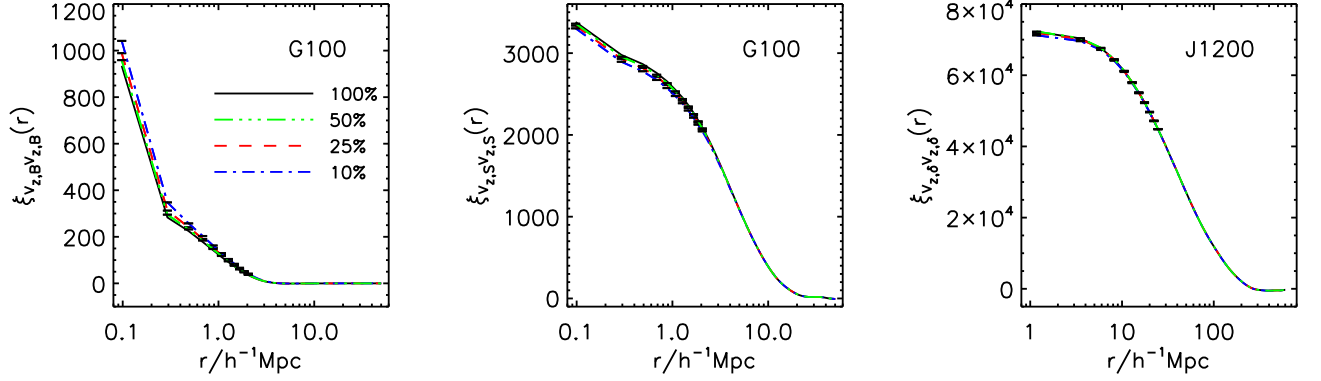


FIG. 15: The velocity correlation functions $\xi_{v_z, \alpha v_z, \alpha}$ of three velocity components calculated using a fraction of randomly selected particles. The error bars are calculated by 10 realizations of randomly selected 50% and 25% particles, and 20 realizations of 10% particles. The data point on the left end of each line is actually $\xi_{v_z, \alpha v_z, \alpha}(r=0) = \sigma_{v_\alpha}^2$.

in $\Delta_{v_B v_B}^2$ at large k in Fig. 14. It is hence challenging to accurately simulate σ_{v_B} . A good thing is that, in our RSD modeling, σ_{v_B} can be chosen as a free parameter to be fitted or even set as zero. So the inability of accurately simulating σ_{v_B} is not a severe problem.

2. Testing against velocity fields of known statistics

The above convergence tests are good at diagnosing and setting up the lower limit of some numerical artifacts. But they can be blind for other artifacts and can

have trouble disentangling various numerical artifacts. A complementary test can be done with a fiducial velocity field of known statistics (in our case the power spectrum). By comparing the measured statistics with the input statistics, errors in the measurement can be quantified straightforwardly. Obviously these errors depend on the fiducial input. So the crucial step for this test is the construction of the input velocity field as realistic as possible. Our proposed velocity decomposition makes this step simpler and more robust. This allows us to perform rigorous tests of the NP method.

First we construct fiducial velocity fields of known

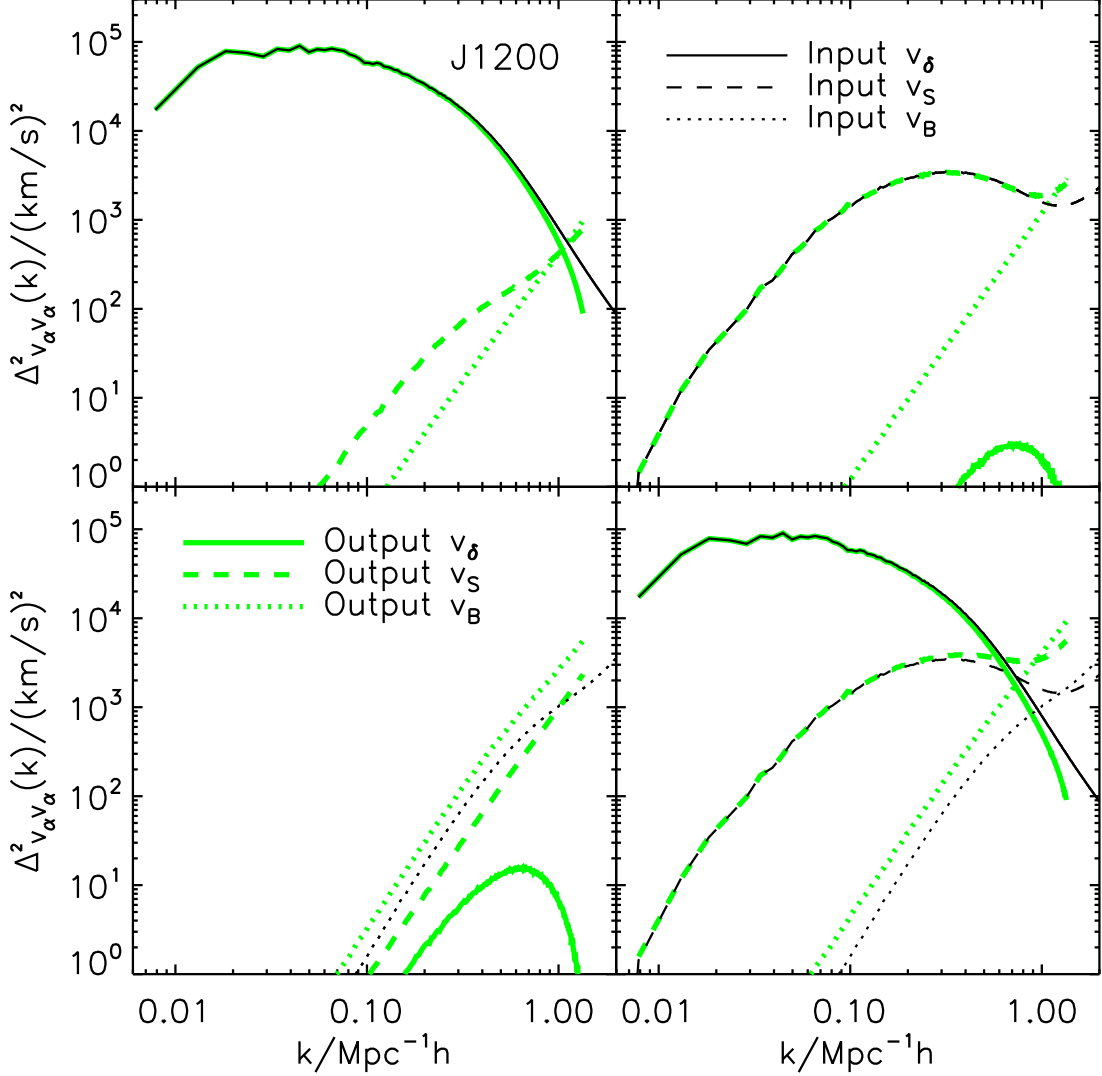


FIG. 16: Test against velocity fields of known statistics in J1200. The input velocity fields are constructed on $N_{\text{grid}} = 1024^3$. The thin black solid, dashed and dotted lines represent input power spectra of \mathbf{v}_δ , \mathbf{v}_S and \mathbf{v}_B respectively. We assign each simulation particle a velocity of its nearest grid point. We then apply the NP method against these “simulations” to measure the output power spectra of \mathbf{v}_δ , \mathbf{v}_S and \mathbf{v}_B , which are shown by thick green solid, dashed and dotted lines respectively. The measurement is performed on $N_{\text{grid}} = 512^3$ grid points. *Top left panel* shows test case A: $\mathbf{v}_\delta \neq 0$ but $\mathbf{v}_S = 0$ and $\mathbf{v}_B = 0$. *Top right panel* shows test case B: $\mathbf{v}_S \neq 0$ but $\mathbf{v}_\delta = 0$ and $\mathbf{v}_B = 0$. *Bottom left panel* shows test case C: $\mathbf{v}_B \neq 0$ but $\mathbf{v}_\delta = 0$ and $\mathbf{v}_S = 0$. *Bottom right panel* shows test case D: $\mathbf{v}_\delta \neq 0$, $\mathbf{v}_S \neq 0$ and $\mathbf{v}_B \neq 0$. These tests clearly show leakages between any two velocity components and hence highlight and quantify these major numerical artifacts. They show that J1200 is robust to measure \mathbf{v}_δ and \mathbf{v}_S at $k \lesssim 0.3h/\text{Mpc}$, where leakages from other velocity components ($\mathbf{v}_S \rightarrow \mathbf{v}_\delta$, $\mathbf{v}_B \rightarrow \mathbf{v}_\delta$, $\mathbf{v}_\delta \rightarrow \mathbf{v}_S$, $\mathbf{v}_B \rightarrow \mathbf{v}_S$) are insignificant. In contrast, leakages from \mathbf{v}_δ and \mathbf{v}_S to \mathbf{v}_B are too severe to measure \mathbf{v}_B by J1200.

statistics on $N_{\text{grid}} = 1024^3$ regular grid points. The fiducial \mathbf{v}_δ is constructed by a combination of measured density field and the best fitted window function $W(k)$ in §IV B, $\theta_\delta(\mathbf{k}) = \delta(\mathbf{k})W(k)$. The fiducial $\mathbf{v}_{S,B}$ can be generated using the measured power spectra, if we assume Gaussianity. Alternatively, we can directly use the measured $\mathbf{v}_{S,B}$ fields by the NP method on regular 1024^3 grid points from our simulations. We will adopt this second approach.

Secondly we assign each particle a velocity, which is the velocity of its nearest grid point. Along with the particle positions from the corresponding simulation (J1200/J300/G100), this is the new “simulation” we use to test our NP method. We will assign these velocities to $N_{\text{grid}} = 512^3$ grid points to do the test. By setting some of the velocity components to zero, we can generate up to seven velocity fields. We have tested the following four cases of them. (A) $\mathbf{v}_\delta \neq 0$ but $\mathbf{v}_S = 0$ and $\mathbf{v}_B = 0$; (B)

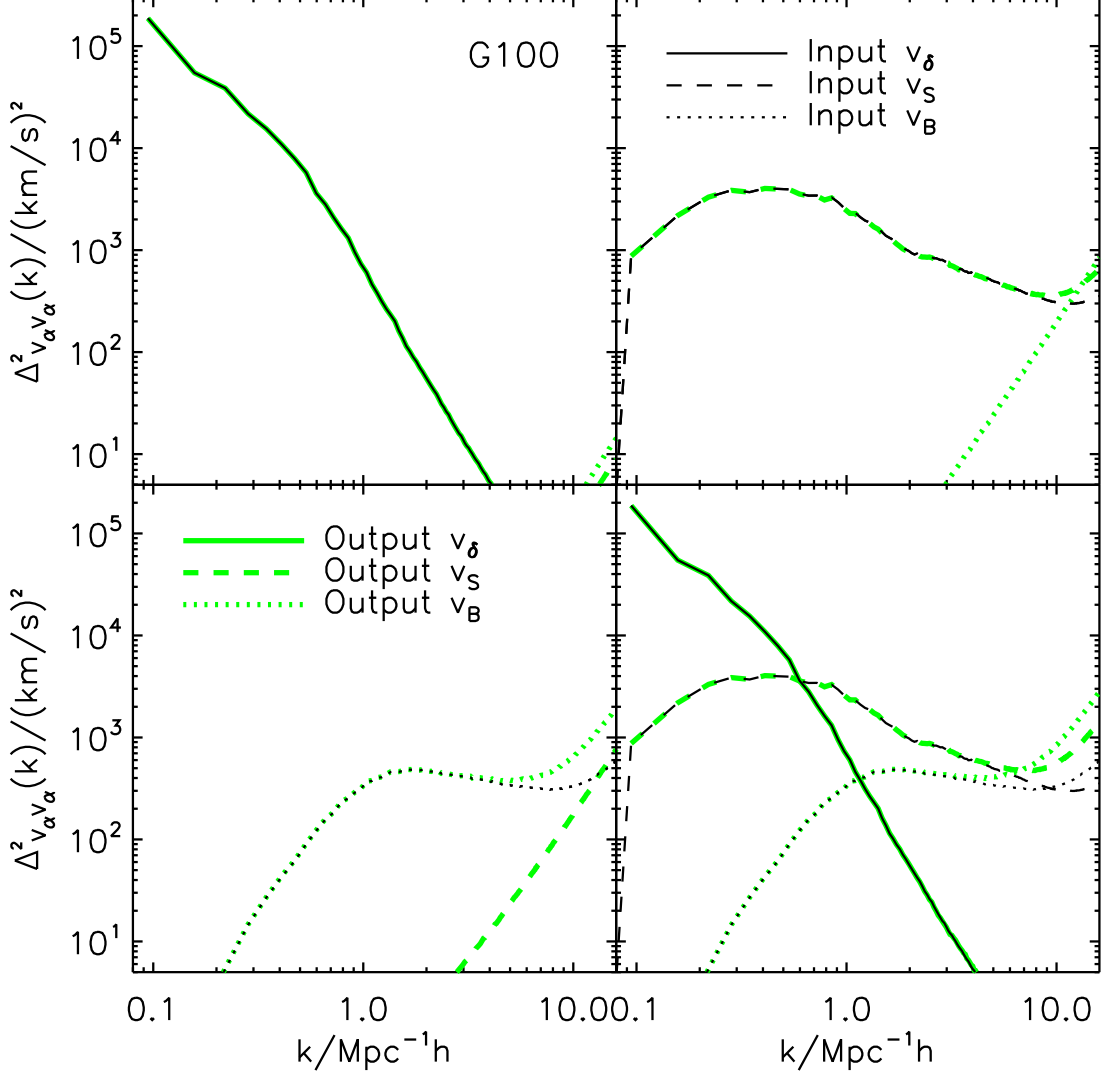


FIG. 17: Same as Fig. 16 except here the test is done in G100. In the *top left panel* the input and output $\Delta_{v_\delta v_\delta}^2$ almost overlap completely, meaning vanishing error in measuring \mathbf{v}_δ by G100. These tests also show that G100 is robust to measure \mathbf{v}_S and \mathbf{v}_B at $k \lesssim 3h/\text{Mpc}$. Leakages between the three velocity components are all well controlled at $k \lesssim 3h/\text{Mpc}$.

$\mathbf{v}_S \neq 0$ but $\mathbf{v}_\delta = 0$ and $\mathbf{v}_B = 0$; (C) $\mathbf{v}_B \neq 0$, but $\mathbf{v}_\delta = 0$ and $\mathbf{v}_S = 0$; and (D) $\mathbf{v}_\delta \neq 0$, $\mathbf{v}_S \neq 0$ and $\mathbf{v}_B \neq 0$.

Tests on J1200 are shown in Fig. 16. (1) First we focus on the measurement accuracy in \mathbf{v}_δ . Test on case A shows that the measured $\Delta_{v_\delta v_\delta}^2$ agrees well with the input one at $k \lesssim 0.4h/\text{Mpc}$ (top left panel, Fig. 16). Tests on case B and C show that the leakages from \mathbf{v}_S and \mathbf{v}_B to \mathbf{v}_δ are negligible. So the measured \mathbf{v}_δ at $k \lesssim 0.4h/\text{Mpc}$ is reliable. This is consistent with the results of convergence tests. (2) For \mathbf{v}_S , more careful interpretation should be given. Test on case B shows that the measured $\Delta_{v_S v_S}^2$ agrees well with the input one at $k \lesssim 0.8h/\text{Mpc}$ (top right panel, Fig. 16). However, tests on case A and case C show that the leakage $\mathbf{v}_\delta \rightarrow \mathbf{v}_S$ and $\mathbf{v}_B \rightarrow \mathbf{v}_S$ are significant. Case D shows that we should only trust the

\mathbf{v}_S measurement at $k \lesssim 0.2h/\text{Mpc}$. This is again consistent with findings through the convergence test. (3) Test on case C shows that the measured $\Delta_{v_B v_B}^2$ agrees with the input one, within a factor of 2 (bottom left panel, Fig. 16). However, this result is very misleading. Tests on case A and B show that most of the output \mathbf{v}_B is caused by the leakage $\mathbf{v}_\delta \rightarrow \mathbf{v}_B$ and $\mathbf{v}_S \rightarrow \mathbf{v}_B$. In other words, \mathbf{v}_B measured in the J1200 simulation is mainly noise, instead of real signal. This is consistent with our previous conclusion based on the convergence tests.

Tests on G100 are shown in Fig. 17. By similar argument, we can draw the conclusion that the NP method is accurate to measure \mathbf{v}_δ and \mathbf{v}_S at $k \sim 1h/\text{Mpc}$. Now the measurement on \mathbf{v}_B is significantly improved, since the leakages $\mathbf{v}_\delta \rightarrow \mathbf{v}_B$ and $\mathbf{v}_S \rightarrow \mathbf{v}_B$ are both subdominant

at $k < 1h/\text{Mpc}$.

These tests can be used to calibrate errors in the velocity measurement. For example, by adding the power

spectra of \mathbf{v}_S and \mathbf{v}_B in case A to that of \mathbf{v}_δ measured from the real data, one can improve the measurement of the \mathbf{v}_δ power spectrum.

-
- [1] P. Zhang, J. Pan, and Y. Zheng, *Phys. Rev. D* **87**, 063526 (2013), 1207.2722.
- [2] J. C. Jackson, *MNRAS* **156**, 1P (1972).
- [3] W. L. W. Sargent and E. L. Turner, *ApJL* **212**, L3 (1977).
- [4] P. J. E. Peebles, *The large-scale structure of the universe* (1980).
- [5] N. Kaiser, *MNRAS* **227**, 1 (1987).
- [6] J. A. Peacock and S. J. Dodds, *MNRAS* **267**, 1020 (1994), arXiv:astro-ph/9311057.
- [7] W. E. Ballinger, J. A. Peacock, and A. F. Heavens, *MNRAS* **282**, 877 (1996), arXiv:astro-ph/9605017.
- [8] J. A. Peacock, S. Cole, P. Norberg, C. M. Baugh, J. Bland-Hawthorn, T. Bridges, R. D. Cannon, M. Colless, C. Collins, W. Couch, et al., *Nature (London)* **410**, 169 (2001), arXiv:astro-ph/0103143.
- [9] M. Tegmark, A. J. S. Hamilton, and Y. Xu, *MNRAS* **335**, 887 (2002), arXiv:astro-ph/0111575.
- [10] M. Tegmark, M. R. Blanton, M. A. Strauss, F. Hoyle, D. Schlegel, R. Scoccimarro, M. S. Vogeley, D. H. Weinberg, I. Zehavi, A. Berlind, et al., *Astrophys. J.* **606**, 702 (2004), arXiv:astro-ph/0310725.
- [11] L. Amendola, C. Quercellini, and E. Giallongo, *MNRAS* **357**, 429 (2005), arXiv:astro-ph/0404599.
- [12] E. V. Linder, *Phys. Rev. D* **72**, 043529 (2005), arXiv:astro-ph/0507263.
- [13] K. Yamamoto, B. A. Bassett, and H. Nishioka, *Physical Review Letters* **94**, 051301 (2005), arXiv:astro-ph/0409207.
- [14] P. Zhang, M. Liguori, R. Bean, and S. Dodelson, *Physical Review Letters* **99**, 141302 (2007), 0704.1932.
- [15] L. Guzzo, M. Pierleoni, B. Meneux, E. Branchini, O. Le Fèvre, C. Marinoni, B. Garilli, J. Blaizot, G. De Lucia, A. Pollo, et al., *Nature (London)* **451**, 541 (2008), 0802.1944.
- [16] Y. Wang, *JCAP* **5**, 21 (2008), 0710.3885.
- [17] W. J. Percival and M. White, *MNRAS* **393**, 297 (2009), 0808.0003.
- [18] Y.-S. Song and W. J. Percival, *JCAP* **10**, 4 (2009), 0807.0810.
- [19] M. White, Y.-S. Song, and W. J. Percival, *MNRAS* **397**, 1348 (2009), 0810.1518.
- [20] Y.-S. Song, *Phys. Rev. D* **83**, 103009 (2011), 1009.2753.
- [21] Y. Wang, W. Percival, A. Cimatti, P. Mukherjee, L. Guzzo, C. M. Baugh, C. Carbone, P. Franzetti, B. Garilli, J. E. Geach, et al., *MNRAS* **409**, 737 (2010), 1006.3517.
- [22] C. Blake, S. Brough, M. Colless, C. Contreras, W. Couch, S. Croom, T. Davis, M. J. Drinkwater, K. Forster, D. Gilbank, et al., *MNRAS* **415**, 2876 (2011), 1104.2948.
- [23] L. Samushia, W. J. Percival, and A. Raccanelli, *MNRAS* **420**, 2102 (2012), 1102.1014.
- [24] C. Blake, S. Brough, M. Colless, C. Contreras, W. Couch, S. Croom, D. Croton, T. Davis, M. J. Drinkwater, K. Forster, et al., ArXiv e-prints (2012), 1204.3674.
- [25] B. A. Reid, L. Samushia, M. White, W. J. Percival, M. Manera, N. Padmanabhan, A. J. Ross, A. G. Sánchez, S. Bailey, D. Bizyaev, et al., ArXiv e-prints (2012), 1203.6641.
- [26] R. Tojeiro, W. J. Percival, J. Brinkmann, J. R. Brownstein, D. Eisenstein, M. Manera, C. Maraston, C. K. McBride, D. Duna, B. Reid, et al., ArXiv e-prints (2012), 1203.6565.
- [27] B. Jain and P. Zhang, *Phys. Rev. D* **78**, 063503 (2008), 0709.2375.
- [28] E. V. Linder, *Astroparticle Physics* **29**, 336 (2008), 0709.1113.
- [29] R. Reyes, R. Mandelbaum, U. Seljak, T. Baldauf, J. E. Gunn, L. Lombriser, and R. E. Smith, *Nature (London)* **464**, 256 (2010), 1003.2185.
- [30] Y.-C. Cai and G. Bernstein, *MNRAS* **422**, 1045 (2012), 1112.4478.
- [31] E. Gaztañaga, M. Eriksen, M. Crocce, F. J. Castander, P. Fosalba, P. Marti, R. Miquel, and A. Cabré, *MNRAS* **422**, 2904 (2012), 1109.4852.
- [32] E. Jennings, C. M. Baugh, B. Li, G.-B. Zhao, and K. Koyama, ArXiv e-prints (2012), 1205.2698.
- [33] B. Li, W. A. Hellwing, K. Koyama, G.-B. Zhao, E. Jennings, and C. M. Baugh, *MNRAS* **428**, 743 (2013), 1206.4317.
- [34] D. Schlegel, F. Abdalla, T. Abraham, C. Ahn, C. Allende Prieto, J. Annis, E. Aubourg, M. Azzaro, S. B. C. Baltay, C. Baugh, et al., ArXiv e-prints (2011), 1106.1706.
- [35] R. Laureijs, J. Amiaux, S. Arduini, J. . Auguères, J. Brinchmann, R. Cole, M. Cropper, C. Dabin, L. Duvet, A. Ealet, et al., ArXiv e-prints (2011), 1110.3193.
- [36] R. Scoccimarro, *Phys. Rev. D* **70**, 083007 (2004), arXiv:astro-ph/0407214.
- [37] U. Seljak and P. McDonald, *JCAP* **11**, 39 (2011), 1109.1888.
- [38] T. Okumura, U. Seljak, P. McDonald, and V. Desjacques, *JCAP* **2**, 10 (2012), 1109.1609.
- [39] T. Okumura, U. Seljak, and V. Desjacques, *JCAP* **11**, 014 (2012), 1206.4070.
- [40] S. Bonoli and U. L. Pen, *MNRAS* **396**, 1610 (2009), 0810.0273.
- [41] V. Desjacques and R. K. Sheth, *Phys. Rev. D* **81**, 023526 (2010), 0909.4544.
- [42] *BigBoss/MS-DESI*, URL <http://bigboss.lbl.gov/>.
- [43] *CHIME*, URL <http://chime.phas.ubc.ca/>.
- [44] *Euclid*, URL <http://www.euclid-ec.org/>.
- [45] *SKA*, URL <http://www.skatelescope.org/>.
- [46] Y. P. Jing, Y. Suto, and H. J. Mo, *Astrophys. J.* **657**, 664 (2007), arXiv:astro-ph/0610099.
- [47] V. Springel, N. Yoshida, and S. D. M. White, *New Astronomy* **6**, 79 (2001), arXiv:astro-ph/0003162.
- [48] V. Springel, *MNRAS* **364**, 1105 (2005), arXiv:astro-ph/0505010.
- [49] F. Bernardeau and R. van de Weygaert, *MNRAS* **279**, 693 (1996).
- [50] R. van de Weygaert and W. Schaap, in *Data Analysis in Cosmology*, edited by V. J. Martínez, E. Saar,

- E. Martínez-González, and M.-J. Pons-Bordería (2009), vol. 665 of *Lecture Notes in Physics, Berlin Springer Verlag*, pp. 291–413.
- [51] S. Pueblas and R. Scoccimarro, *Phys. Rev. D* **80**, 043504 (2009), 0809.4606.
- [52] F. Bernardeau, S. Colombi, E. Gaztañaga, and R. Scoccimarro, *Physics reports* **367**, 1 (2002), arXiv:astro-ph/0112551.
- [53] C.-H. Chuang, F. Prada, A. J. Cuesta, D. J. Eisenstein, E. Kazin, N. Padmanabhan, A. G. Sanchez, X. Xu, F. Beutler, M. Manera, et al., *ArXiv e-prints* (2013), 1303.4486.
- [54] B. A. Reid, L. Samushia, M. White, W. J. Percival, M. Manera, N. Padmanabhan, A. J. Ross, A. G. Sánchez, S. Bailey, D. Bizyaev, et al., *MNRAS* **426**, 2719 (2012), 1203.6641.
- [55] R. Tojeiro, W. J. Percival, J. Brinkmann, J. R. Brownstein, D. J. Eisenstein, M. Manera, C. Maraston, C. K. McBride, D. Muna, B. Reid, et al., *MNRAS* **424**, 2339 (2012), 1203.6565.
- [56] E. Macaulay, I. Kathrine Wehus, and H. K. Eriksen, *ArXiv e-prints* (2013), 1303.6583.
- [57] S. Cole, K. B. Fisher, and D. H. Weinberg, *MNRAS* **275**, 515 (1995), arXiv:astro-ph/9412062.
- [58] A. Diaferio and M. J. Geller, *Astrophys. J.* **467**, 19 (1996), arXiv:astro-ph/9602086.
- [59] B. C. Bromley, M. S. Warren, and W. H. Zurek, *Astrophys. J.* **475**, 414 (1997), arXiv:astro-ph/9701177.
- [60] X. Kang, Y. P. Jing, H. J. Mo, and G. Börner, *MNRAS* **336**, 892 (2002), arXiv:astro-ph/0201124.
- [61] Y. P. Jing, *Astrophys. J.* **620**, 559 (2005), arXiv:astro-ph/0409240.
- [62] J. Koda, C. Blake, T. Davis, M. Scrimgeour, G. B. Poole, and L. S. Smith, *ArXiv e-prints* (2013), in preparation.
- [63] W. Cui, L. Liu, X. Yang, Y. Wang, L. Feng, and V. Springel, *Astrophys. J.* **687**, 738 (2008), 0804.0070.
- [64] For the galaxy field, $W_g \rightarrow \beta \equiv f/b_g$ in the limit $k \rightarrow 0$. Refer to paper I for detailed discussions.
- [65] This is a rough estimation based on the approximation $f \sim \Omega_m^{1/2}(z) \propto \sqrt{\Omega_m(1+z)^3}/H^2$ and $D \sim (1+z)^{-1}$. Under these approximations, we have $fHD \propto (1+z)^{1/2}$.
- [66] J. Koda kindly showed us their ongoing work [62], which also proposed the NP method. This work also quantified and corrected the alias effect of the NP method.
- [67] The Delaunay Tessellation (DT) velocity assignment utilizes a two-step scheme to get a volume-weighted velocity field: first it produces a Delaunay tessellation by linking the closest 4 particles to form a tetrahedron network. The velocity field inside one tetrahedron is determined through linearly interpolating the velocities at its 4 vertices. Then the velocity field is smoothed over a given window function to obtain the velocities on regular grids. The DT method has been proved to be accurate and reliable at linear and quasi-linear scales (e.g. [49–51]). However it breaks down at nonlinear regimes where shell-crossings and multi-stream flows occur [50]. In these regions, the linear interpolation tends to underestimate the velocity by averaging velocities with different directions. The smoothing procedure further smoothes out random (but real) motions at small scales. Since most contribution to \mathbf{v}_S and \mathbf{v}_B comes from nonlinear scales, the DT method could significantly underestimate \mathbf{v}_S and \mathbf{v}_B .
- [68] The sign of \mathbf{v}_δ expression being plus or minus depends on the definition of Fourier transform. Our definition for Fourier transform is $\delta(\mathbf{k}) \equiv \int \delta(\mathbf{x}) \exp(i\mathbf{k} \cdot \mathbf{x}) d^3x$.